Comparing observations and parameterizations of ice-ocean drag through an annual cycle across the Beaufort Sea

Samuel Brenner [1], Luc Rainville [1], Jim Thomson [1], Sylvia Cole [2], Craig Lee [1]

[1]Applied Physics Laboratory, University of Washington, Seattle, WA, USA
[2]Woods Hole Oceanographic Institution, Woods Hole, MA, USA

Key Points:

- In-situ measurements are used to estimate ice-ocean drag across a wide range of ice conditions based on the sea ice momentum balance.
- Ice-ocean drag coefficients show a seasonal cycle with a spring maximum and a fall minimum, following the growth and melt of ice keels.
- Geometry-based drag parameterization schemes are able to capture much of the observed variability using direct ice geometry measurements.

Corresponding author: Samuel Brenner, `sdbren@uw.edu`

Abstract

Understanding and predicting sea ice dynamics and ice-ocean feedback processes requires accurate descriptions of momentum fluxes across the ice-ocean interface. In this study, we present observations from an array of moorings in the Beaufort Sea. Using a force-balance approach, we determine ice-ocean drag coefficient values over an annual cycle and a range of ice conditions. Statistics from high resolution ice draft measurements are used to calculate expected drag coefficient values from morphology-based parameterization schemes. With both approaches, drag coefficient values ranged from approximately $1–10\times10^{-3}$, with a minimum in fall and a maximum at the end of spring, consistent with previous observations. The parameterizations do a reasonable job of predicting the observed drag values if the under ice geometry is known, and reveal that keel drag is the primary contributor to the total ice-ocean drag coefficient. When translations of bulk model outputs to ice geometry are included in the parameterizations, they overpredict drag on floe edges, leading to the inverted seasonal cycle seen in prior models. Using these results to investigate the efficiency of total momentum flux across the atmosphere-ice-ocean interface suggests an inter-annual trend of increasing coupling between the atmosphere and the ocean.

Plain Language Summary

Sea ice moves in response to the push and pull (a.k.a., "drag') of both wind and ocean currents, so speeds of both the ice and the underlying ocean depends on how efficient that drag is. By looking at measurements of ice motion in response to the wind and ocean currents from three sites in the Beaufort Sea, we have calculated drag efficiency over one year. Computer models predict drag efficiency based on how rough the bottom of the sea ice is. Our measurements of the shape of the sea ice bottom are used to test and verify the framework for calculating drag efficiency that is in place in those models. The model framework can do a reasonable job of prediction if given good measurements of how rough the ice is, but may not be good at predicting that roughness. Because of that, current models might overpredict the drag efficiency while ice is melting. With our measurements of drag efficiency, we calculate how the sea ice impacts the total ability of the wind to push on the ocean and find that it is enhanced by the sea ice. As Arctic sea ice becomes more seasonal, we expect this enhancement to increase.

1 Introduction

Ongoing and dramatic changes in Arctic sea ice (e.g., Stroeve & Notz, 2018) and the underlying ocean (Jackson et al., 2011; Timmermans et al., 2018; Armitage et al., 2020) highlight the need to understand Arctic system feedback processes. Sea ice dynamics are thought to play an important role in both localized (e.g., Ivanov et al., 2016) and large-scale ice-ocean feedbacks (Dewey et al., 2018; Meneghello et al., 2018; Armitage et al., 2020). However, there are still fundamental gaps in our knowledge of the role of sea ice in mediating momentum transfer across the atmosphere-ice-ocean system, especially in understanding spatial and seasonal variability in ice-ocean drag.

Turbulent processes in the ocean and in the atmosphere drive surface momentum flux (a.k.a., stress) across the ice-ocean and ice-atmosphere interfaces. These turbulent fluxes are commonly related to bulk quantities through quadratic drag laws; e.g., the ice-ocean stress, $\boldsymbol{\tau}_{io}$, and atmosphere-ice stress, $\boldsymbol{\tau}_{ai}$:

$$\boldsymbol{\tau}_{io} = \rho_o C_{io} e^{i\beta} \boldsymbol{u}_{rel} \left| \boldsymbol{u}_{rel} \right|, \tag{1a}$$

$$\boldsymbol{\tau}_{ai} = \rho_a C_{ai} \boldsymbol{u}_a \left| \boldsymbol{u}_a \right|, \tag{1b}$$

which depend on ice-ocean and atmosphere-ice drag coefficients: C_{io} and C_{ai}, respectively (the relative ice-ocean horizontal velocity $\boldsymbol{u}_{rel} = \boldsymbol{u}_i - \boldsymbol{u}_o$ and vectors are written in complex notation, e.g. $\boldsymbol{u} = u + iv$; for other variable definitions, see table 1). While there has been considerable work in relating observed values of the atmosphere-ice drag coefficient, C_{ai}, to sea ice properties (Arya, 1975; Guest & Davidson, 1987; Lüpkes & Birnbaum, 2005; Andreas, Horst, et al., 2010; Andreas, 2011; Lüpkes et al., 2012; Castellani et al., 2014; Elvidge et al., 2016; Petty et al., 2017, and others), there is relatively little analogous work on the ice-ocean drag coefficient, C_{io}. Indeed, despite a wide range of observed values of C_{io} spanning across an order of magnitude (e.g., McPhee, 1980; Morison et al., 1987; McPhee, 2002; Shaw et al., 2008; Randelhoff et al., 2014; Cole et al., 2014, 2017), by default many sea ice models use a constant value for the drag coefficient (e.g., Köberle & Gerdes, 2003; Timmermann et al., 2009; Losch et al., 2010; Rousset et al., 2015; Rampal et al., 2016), such as the "canonical" value of $C_{io} = 5.5 \times 10^{-3}$ determined by McPhee (1980). Moreover, studies show that modelled sea ice thickness is sensitive to the chosen value of C_{io} (J. G. Kim et al., 2006; Hunke, 2010).

Recent observations show both spatial and seasonal variations in the ice-ocean drag coefficient (Cole et al., 2017), suggesting the importance of ice morphology on the values of C_{io} (e.g., due to form drag; Steele et al., 1989; Lu et al., 2011; Tsamados et al., 2014). Model studies that incorporate a variable ice-ocean drag via parametrization of form drag (directly, Tsamados et al., 2014; or indirectly, Steiner, 2001) show first-order impacts both on the sea ice (Castellani et al., 2018) and the underlying ocean (Martin et al., 2016; Castellani et al., 2015, 2018). Although form drag parameterizations of the ice-ocean drag provide a nice theoretical description for the relationship between sea ice morphology and the ice-ocean drag coefficient(Lu et al., 2011; Tsamados et al., 2014), until now there has been no detailed observational study comparing morphological features with observed values of C_{io} across a range of sea ice conditions.

In this study, we present observations made over an annual cycle from an array of moorings in the Beaufort Sea. Using a force-balance approach, mooring measurements and atmospheric re-analysis data are used to infer ice-ocean drag coefficients. Uplooking sonar on the moorings provide snapshots of under-ice topography and statistics related to ice keels and floe edges. Together, these results 1) provide insight into the morphological drivers underlying variations of the ice-ocean drag coefficient, 2) are used for evaluation of model parameterization schemes, and 3) provide context for a broader understanding of momentum transfer into the upper ocean in the changing Arctic. The remainder of this paper is organized as follows: sections 1.1 and 1.2 provide additional background about momentum fluxes across the atmosphere-ice-ocean interface (with focus on the sea ice momentum equation and the total atmosphere-ocean momentum flux). Section 2 provides a review of the geometry-based parameterization schemes developed by Lu et al. (2011) and Tsamados et al. (2014), thus giving important context for interpreting the study results. In section 3 we describe the field study and measurements, along with the force-balance and geometry-based descriptions of the ice-ocean drag coefficient. Descriptions of variations in C_{io}, along with evaluation of the parameterization schemes, and a description of the morphological drivers of ice-ocean drag are presented in section 4. Then, in section 5, these results are placed in the context of previous observations of ice-ocean drag and total momentum flux. The main contributions of the study are summarized in section 6.

1.1 The sea ice momentum equation

The conservation of momentum of sea ice can be written as (e.g., Leppäranta, 2011; modified to account for mixed ice-open water conditions per Hunke & Dukowicz, 2003;

Table 1: Notation

a_i	ice covered area	m_w	skin drag attenuation parameter
a_{rdg}	area covered in ridged ice	P_0	boundary-layer integration function
b_1, b_2, A_*	geometry parameters	S_c	sheltering function
A	ice concentration	s_l	attenuation parameter
c_f	local floe-edge drag coefficient	$\boldsymbol{u}_*$	friction velocity
c_k	local keel drag coefficient	$\boldsymbol{u}_a$	wind velocity at 10 m
c_s	local skin drag coefficient	$\boldsymbol{u}_i$	ice drift velocity
C_f	form drag from floe edges	$\boldsymbol{u}_o$	ocean velocity at a reference depth
C_k	form drag from keels	$\boldsymbol{u}_g$	geostrophic ocean velocity
C_s	skin drag	$\boldsymbol{u}_{rel}$	ice-ocean relative velocity
C_{ao}	atmosphere-ocean drag coefficient	v_{rdg}	volume of ridged ice
C_{ai}	atmosphere-ice drag coefficient	z_0	roughness length
C_{io}	ice-ocean drag coefficient	z_{0i}	roughness length of level ice
C_{equiv}	atmosphere-ocean equivalent drag	z_{0w}	roughness length water
d_i	ice draft	z_{ref}	reference depth
d_{lvl}	level ice draft	β	turning angle
f	Coriolis parameter	η	sea surface displacement
$\boldsymbol{F}_a$	ice acceleration force	κ	von Kármán constant
$\boldsymbol{F}_i$	ice interaction force	ρ_a	air density
g	gravitational acceleration	ρ_i	ice density
h_i	ice thickness	ρ_o	ocean density
h_k	keel depth	$\boldsymbol{\sigma}$	internal ice stress tensor
$h_{k\mathrm{rel}}$	relative keel depth	$\boldsymbol{\tau}_{ai}$	atmosphere-ice stress
$h_{k\mathrm{tot}}$	total keel depth	$\boldsymbol{\tau}_{ao}$	atmosphere-ocean stress
ℓ_f	floe length	$\boldsymbol{\tau}_{io}$	ice-ocean stress
ℓ_k	keel spacing	$\boldsymbol{\tau}_{oi}$	ocean-ice stress
ℓ_l	lead length	$\boldsymbol{\tau}_{ocn}$	total ocean stress
m_e	effective ice mass per unit area	$\boldsymbol{\tau}_{atm}$	total atmosphere stress

Connolley, Gregory, Hunke, & Mclaren, 2004):

$$m_e\left[\underbrace{\frac{\partial \boldsymbol{u}_i}{\partial t}}_{\mathrm{I}} + \underbrace{\boldsymbol{u}_i \cdot \nabla \boldsymbol{u}_i}_{\mathrm{II}} + \underbrace{f\hat{k} \times \boldsymbol{u}_i}_{\mathrm{III}}\right] = \underbrace{A\boldsymbol{\tau}_{ai}}_{\mathrm{IV}} + \underbrace{A\boldsymbol{\tau}_{oi}}_{\mathrm{V}} + \underbrace{\nabla \cdot \boldsymbol{\sigma}}_{\mathrm{VI}} + \underbrace{m_e g \nabla \eta}_{\mathrm{VII}}, \tag{2}$$

for m_e the "effective" ice mass per unit area, $m_e = A\rho_i h_i$, and other variables as defined in table 1, with ∇ the horizontal gradient operator. The terms of the equation are as follows: (I) local ice acceleration; (II) advective ice acceleration; (III) Coriolis acceleration; (IV) stress of the atmosphere acting on the ice; (V) stress of the ocean acting on the ice; (VI) internal stress ("ice-ice" stress); and (VII) gravitational force from sea surface tilt. Advective acceleration (term II) is generally considered negligible and excluded. The final term (VII) in eq. (2) can be expressed in terms of the geostrophic balance $f\hat{k} \times \boldsymbol{u}_g = g\nabla\eta$ and then combined with the Coriolis term, so that term III becomes $f\hat{k} \times (\boldsymbol{u}_i - \boldsymbol{u}_g)$ (Leppäranta, 2011). An additional term representing wave radiation stress in the marginal ice zone has been shown to be locally important at the ice edge (e.g., Perrie & Hu, 1997; Steele et al., 1989), but overall is small, so it is neglected. Leppäranta (2011) also includes an atmospheric pressure gradient term which is not included here. In mixed ice-open water conditions, the ocean-ice and atmosphere-ice stresses ($\boldsymbol{\tau}_{ai}$ and $\boldsymbol{\tau}_{oi}$) represent the stress acting only on the ice-covered area and are distinct from the total stress out of the ocean/atmosphere (Hunke & Dukowicz, 2003).

Sea ice is considered to be in "free drift" if the internal ice stress (term VI) is negligible (e.g., McPhee, 1980; Hunke & Dukowicz, 2003; Connolley et al., 2004; Leppäranta, 2011). This is often assumed to be the case if the ratio of ice speed to wind speed ($|\boldsymbol{u}_i|/|\boldsymbol{u}_a|$, the "wind factor") is sufficiently high (typically $\geq$2%; e.g., McPhee, 1980), or if ice concentration is sufficiently low (e.g., $\leq$85%; Hunke & Dukowicz, 2003; Heorton et al., 2019). For freely drifting sea ice, the ice-ocean stress ($\boldsymbol{\tau}_{io} = -\boldsymbol{\tau}_{oi}$) can be expressed as:

$$\boldsymbol{\tau}_{io} = \boldsymbol{\tau}_{ai} - \rho_o d_i \left[\frac{\partial \boldsymbol{u}_i}{\partial t} + f\hat{k} \times (\boldsymbol{u}_i - \boldsymbol{u}_g)\right], \tag{3}$$

where the sea ice mass per unit area $\rho_i h_i$ (for ice density ρ_i and total ice thickness h_i) been replaced with $\rho_o d_i$ (for ocean density ρ_o and ice draft d_i) assuming hydrostatic balance. McPhee (1980) and Dewey (2019) use this balance, assuming steady-state ($\frac{\partial \boldsymbol{u}_i}{\partial t} = 0$), in order to calculate ice-ocean stress and infer the ice-ocean drag coefficient, while Randelhoff et al. (2014) employ this equation retaining the local acceleration. The ice-ocean stress is also frequently presented in terms of friction velocity, u_*, defined by $\boldsymbol{\tau}_{io} = \rho_o \boldsymbol{u}_* |\boldsymbol{u}_*|$.

1.2 Total momentum flux into the ocean

In mixed ice and open-water conditions, there is both a direct transfer of momentum between the atmosphere and the ocean, and an indirect transfer mediated by sea ice. It is common to represent these fluxes as combinations of the corresponding atmosphere-ice-ocean stresses weighted by sea ice concentration (e.g., Martin et al., 2014, 2016). Then, the total momentum flux into the ocean, $\boldsymbol{\tau}_{ocn}$, and the total momentum flux out of the atmosphere $\boldsymbol{\tau}_{atm}$ can be represented as:

$$\boldsymbol{\tau}_{ocn} = A\boldsymbol{\tau}_{io} + (1-A)\boldsymbol{\tau}_{ao}, \quad \text{and} \tag{4a}$$

$$\boldsymbol{\tau}_{atm} = A\boldsymbol{\tau}_{ai} + (1-A)\boldsymbol{\tau}_{ao}, \tag{4b}$$

where A is sea ice concentration, and each of the stress components (ice-ocean: $\boldsymbol{\tau}_{io}$; atmosphere-ice: $\boldsymbol{\tau}_{ai}$; atmosphere-ocean: $\boldsymbol{\tau}_{ao}$) is described by the quadratic drag law with corresponding drag coefficients: $\boldsymbol{\tau}_{ao} = \rho_a C_{ao} \boldsymbol{u_a} |\boldsymbol{u_a}|$, and $\boldsymbol{\tau}_{io}$, $\boldsymbol{\tau}_{ai}$ from eqs. (1a) and (1b). As a first approximation, the atmosphere-ocean drag coefficient, C_{ao}, can be described as a function of wind speed (e.g., Large & Yeager, 2004). The atmosphere-ice drag coefficient, C_{ai}, is expected to depend on sea ice geometry in a similar way to the ice-ocean drag (Andreas, 2011; Lüpkes et al., 2012; Tsamados et al., 2014); however, it is commonly parameterized simply as a function of ice concentration, A (see supporting information Text S2).

Combining eqs. (2), (4a) and (4b) leads to the expression:

$$\boldsymbol{\tau}_{ocn} = \boldsymbol{\tau}_{atm} + \boldsymbol{F}_i + \boldsymbol{F}_a, \tag{5}$$

where $\boldsymbol{F}_i$ is the ice interaction force (derived from the inclusion of term VI in eq. 2), and $\boldsymbol{F}_a$ is the equivalent force from the acceleration and tilt terms (terms I, III, VII in eq. 2; i.e., the term in brackets in eq. 3). Equation (5) mirrors the expression from Martin et al. (2014, their equation 2), except for the inclusion of the equivalent forces from ice acceleration, $\boldsymbol{F}_a$, which they neglect.

In the scenario where the transfer of momentum is an overall flux from the atmosphere into the ocean, this equation can been interpreted to state that all of the momentum flux out of the atmosphere ($\boldsymbol{\tau}_{atm}$) goes into either the ice ($\boldsymbol{F}_i + \boldsymbol{F}_a$), or into the ocean ($\boldsymbol{\tau}_{ocn}$). Although, because of the vector summation in eq. (5), both of $\boldsymbol{F}_i$ and $\boldsymbol{F}_a$ can either enhance or subtract from $\boldsymbol{\tau}_{atm}$. Ice interaction is usually thought as a momentum sink that opposes $\boldsymbol{\tau}_{atm}$ (Steele et al., 1997; Martin et al., 2014), but ice acceleration terms could potentially be an additional source of ocean momentum.

To examine the effect of sea ice in mediating the total momentum flux from the atmosphere to the ocean, consider an "equivalent drag coefficient", C_{equiv}, based on the construction of a quadratic drag law between the wind speed and the total ocean stress; i.e.,

$$C_{equiv} = \frac{|\boldsymbol{\tau}_{ocn}|}{\rho_a |\boldsymbol{u}_a|^2}. \tag{6}$$

C_{equiv} does not have a clean analytic form, nor is it a useful prognostic variable: its value will depend on $\boldsymbol{u}_i$ and $\boldsymbol{u}_o$, which are themselves functions of the total atmosphere-ice-ocean momentum transfer. Instead, C_{equiv} is a diagnostic of momentum transfer efficiency, where higher values indicate that a greater proportion of atmospheric momentum is ultimately transferred to the ocean. This is similar to the use of a normalized effective stress in Martin et al. (2014, 2016).

2 Drag from geometry-based parameterizations

This study compares estimates of the observed ice-ocean drag to two schemes that parameterize the ice-ocean drag as a function of the observable ice geometry. Both Lu et al. (2011) and Tsamados et al. (2014) present similar ice geometry-based parameterizations of the ice-ocean drag coefficient based on a combination of skin and form drag components, with the scheme by Tsamados et al. (2014) available in the CICE sea ice model (Hunke et al., 2020). Steiner (2001) presents an alternative scheme using a "deformation energy" approach. That method has been used in the sea ice component of the MITgcm model (Losch et al., 2010) to investigate the impact of variable ice-ocean drag (Castellani et al., 2018); however, we cannot track deformation energy with our measurements, so that scheme is not considered here.

2.1 Details of parameterization schemes

Ice-geometry based parameterizations of the ice-ocean drag coefficient write the total drag as a sum of form drag from floe edges, form drag from keels, and skin drag (Lu et al., 2011; Tsamados et al., 2014):

$$C_{io} = C_f + C_k + C_s. \tag{7}$$

For both schemes, these three drag components can be written as:

$$\text{floe edge drag:} \qquad C_f = \frac{1}{2} c_f A \frac{d_{lvl}}{\ell_f} \left[S_c \left(\frac{d_{lvl}}{\ell_l} \right) \right]^2 P_0(d_{lvl}, z_{0w}), \tag{8a}$$

$$\text{keel drag:} \qquad C_k = \frac{1}{2} c_k A \frac{h_k}{\ell_k} \left[S_c \left(\frac{h_k}{\ell_k} \right) \right]^2 P_0(h_k, z_{0i}), \tag{8b}$$

$$\text{skin drag:} \qquad C_s = c_s A \left(1 - m_w \frac{h_k}{\ell_k} \right), \quad \text{if } \frac{h_k}{\ell_k} \leq \frac{1}{m_w} \tag{8c}$$

with variables defined in table 1. So the ice geometry appears in the parametrizations as the floe "aspect ratio", d_{lvl}/ℓ_f, and the "ridging intensity", h_k/ℓ_k. The scheme by Tsamados et al. (2014) is an adaptation of an atmospheric drag parameterization by Lüpkes et al. (2012). Note that in Tsamados et al. (2014), the inequality in the valid range for the skin drag, C_s ($h_k/\ell_k \leq 1/m_w$), is mistakenly reversed (compare their equation 19 with the work of Arya, 1975 on which skin drag is based); eq. (8c) presents the correct inequality for both of the parameterization schemes.

The two schemes are functionally similar. The differences between them are due to the following factors: (1) different values of the "local" drag coefficients, c_f, c_k, and c_s (which account for the drag on individual elements); (2) different forms the "sheltering functions" S_c; and (3) the inclusion (or not) of the functions P_0 (which are included in the Tsamados et al., 2014 scheme but not the Lu et al., 2011 scheme). Additionally, the two schemes use slightly different definitions for keel depth (relative versus total; see fig. 1).

The sheltering function S_c accounts for the reduction in drag of downstream obstacles due to the wake effect of upstream obstacles (Steele et al., 1989). Both parameterization schemes employ different, empirically-derived, sheltering functions:

$$\text{Tsamados et al. (2014):} \qquad S_c(x) = \left[1 - \exp\left(-\frac{s_l}{x} \right) \right]^{1/2} \tag{9a}$$

$$\text{Lu et al. (2011):} \qquad S_c(x) = \left[1 - (x)^{1/2} \right] \tag{9b}$$

For keel sheltering, the input argument, x, is the the ridging intensity, h_k/ℓ_k, which mirrors its other use eq. (8b). For floe sheltering, the argument for the sheltering function is d_{lvl}/ℓ_l (the denominator is the distance between floes), instead of the aspect ratio d_{lvl}/ℓ_f that appears earlier in eq. (8a).

Tsamados et al. (2014) include a term in C_f and C_k which arises due to integration of a depth-varying velocity profile over the height of an obstacle, here called P_0 (it differs from the definition of P_0 in Lüpkes et al., 2012). In the atmospheric drag parameterization, Lüpkes et al. (2012) assume a "law-of-the-wall" velocity profile: $u(z) = (u_*/\kappa)\ln(z/z_0)$, which Tsamados et al. (2014) maintains in adapting the scheme to the ice-ocean boundary layer. This gives

$$P_0(h, z_0) = \left[\frac{\ln(h/z_0)}{\ln(z_{\text{ref}}/z_0)}\right]^2. \tag{10}$$

Inclusion of P_0 allows the ice-ocean drag coefficient to be an explicit function of the reference depth z_{ref}. For the range of measurements and parameters in the present study P_0 varied from ∼0.3–0.8. The form of P_0 depends on the assumed law-of-the-wall boundary-layer structure, which is suitable for the atmosphere where the height of logarithmic boundary layer is on the order of hundreds of meters (Holton, 2004, chapter 5). However, it is not clear that this is appropriate in the ice-ocean boundary layer. The P_0 functions are not included in the scheme by Lu et al. (2011).

The "local" drag coefficient, c_s used in the skin drag parameterization (C_s, eq. 8c) represents the baseline skin drag associated with level ice in the absence of ridges. Both Tsamados et al. (2014) and Lu et al. (2011) treat this term as a free parameter. Keeping with the law-of-the-wall velocity assumption used to develop P_0, the baseline skin drag could instead be represented by

$$c_s = \left[\frac{\kappa}{\ln(z_{\text{ref}}/z_{0i})}\right]^2, \tag{11}$$

thus reducing the number of free parameters in the model, and allowing c_s to be an explicit function of the reference depth z_{ref}. As with P_0, the actual form will depend strongly on boundary layer structure.

In applying their parametrization scheme (eqs. 8, 9a, and 10), Tsamados et al. (2014) use total keel depth, $h_{k\text{tot}}$, which is measured from the waterline (fig. 1). However, in full ice cover, it should be the keel depth relative to the level ice draft, $h_{k\text{rel}}$, that contributes to form drag (as in Lu et al., 2011). Similarly, the reference depth z_{ref} in eqs. (10) and (11) should be also be relative to the level ice draft (e.g., $z_{\text{ref}} - d_{lvl}$), because that is the range over which the boundary layer develops. In mixed ice-open water conditions, the use of $h_{k\text{rel}}$ is still consistent with the parametrization scheme as floe-edge drag (eq. 8a) is accounted for separately.

2.2 Translating model outputs to ice geometry

The details of sea ice geometry necessary for calculating the ice-ocean drag coefficient with eq. (8) are not generally resolved by models, which don't simulate individ-

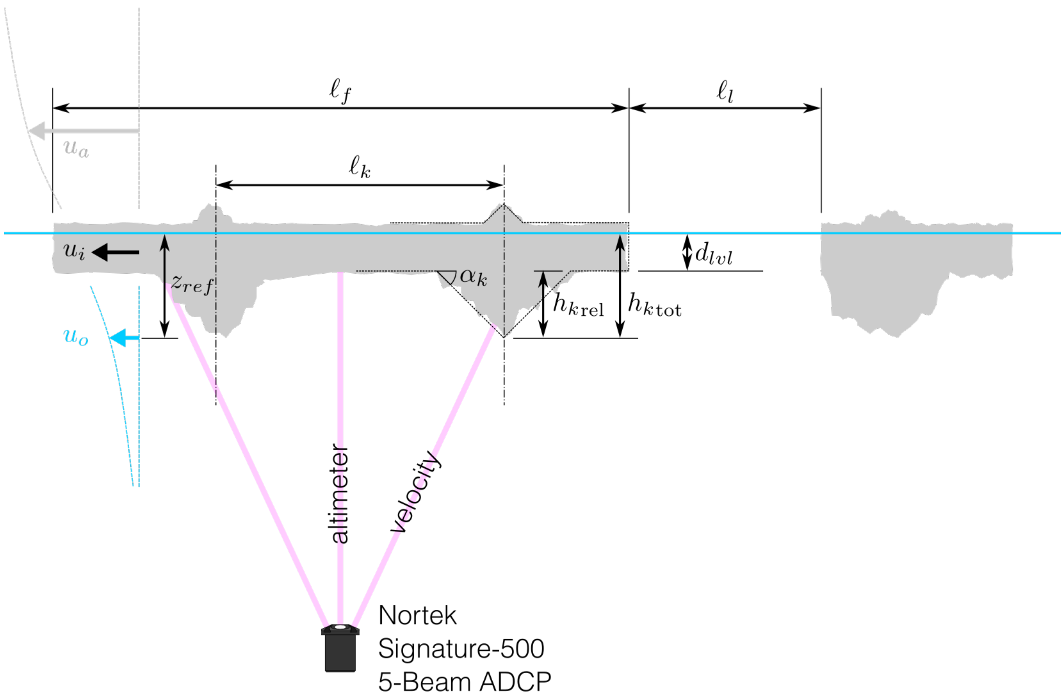

Figure 1: Schematic representation of an ice floe showing sea ice geometry with idealized triangular representation of ice keels, and the in-situ ADCP measurements. Dimension labels of ice geometry correspond to table 1.

ual ice floes or keels. Tsamados et al. (2014) developed a scheme for estimating average keel properties based on outputs in the CICE model using assumptions about the keel geometry that are guided by observations (see their supplementary information). Namely, the scheme uses area extent and volume of ridged ice in a model grid cell (a_{rdg} and v_{rdg}, respectively), along with the ice area in a grid cell (a_i, which is the ice concentration A multiplied by the grid-cell area).

For subsurface measurements (as presented below), keel height and spacing are given by taking the limit as $R_h \rightarrow \infty$ in equations 24 and 25 from Tsamados et al. (2014) (where R_h is the ratio of keel depth to sail height, so the limit states that all ridged ice in the measurements is attributed to keels). This gives the expressions:

$$h_k = 2\frac{v_{rdg}}{a_{rdg}}\frac{b_1}{\phi_k}, \tag{12a}$$

$$\ell_k = 2h_k\frac{a_i}{a_{rdg}}\frac{b_1}{\tan(\alpha_k)}, \tag{12b}$$

where b_1 is a weight function accounts for the overlap of keels with level ice (taken as 0.75), ϕ_k is the keel porosity, and α_k is the keel slope (see fig. 1).

The floe and lead lengths (ℓ_f, ℓ_l) used in eq. (8a) are also parameterized. Using measurements derived from aerial photographs of the marginal ice zone of Fram Strait, Lüpkes et al. (2012) developed an empirical model for estimating floe size based on ice concentration:

$$\ell_f = \ell_{f,max}\left(\frac{A_*}{A_* - A}\right)^{b_2}, \tag{13}$$

with b_2 a tunable parameter (ranging from 0.3 to 1.4), and A_* a value calculated such that the limits of ℓ_f range from $\ell_{f,min}$ to $\ell_{f,max}$ (for $A \rightarrow 0, 1$), the minimum and maximum floe lengths, respectively (see eq. 27 in Lüpkes et al., 2012). Using default parameters, this gives average floe lengths that are limited to range from a minimum of 8 m to a maximum of 300 m. Tsamados et al. (2014) implement this floe size model in their parametrization scheme, though they acknowledge that observations have shown that floe size follows a power-law distribution with a much wider range of scales than is possible with that scheme (e.g., Weiss & Marsan, 2004; see also Stern, Schweiger, Zhang, & Steele, 2018 and references therein).

3 Drag from field measurements

3.1 Field measurements

Data were collected during the Stratified Ocean Dynamics of the Arctic (SODA) experiment: an Office of Naval Research (ONR) project to better understand the controls of heat and momentum transfer in the Arctic's upper ocean. A program component included the installation of three subsurface moorings in a line stretching from the south to the north of the Beaufort Sea, which are designated as SODA-A, SODA-B, and SODA-C (figs. 2a and 2b). The moorings recorded a full annual cycle of sea ice growth and melt from their installation in fall 2018 to their recovery in fall 2019. The spatial distribution of the moorings allowed for sampling of different ice regimes: the southernmost mooring (SODA-A) was in the seasonal ice zone and experiences prolonged open-water periods in summer (fig. 2e); SODA-B was near the edge of the seasonal ice zone and has a minimal open-water period but a longer period of time in marginal ice (fig. 2d); whereas SODA-C was still ice-covered all year long (fig. 2c; the mooring at that location was both deployed and recovered through the ice).

This study utilizes measurements made with uplooking Nortek Signature-500 5-beam acoustic Doppler current profilers (ADCPs) installed on the top float of each mooring (fig. 1). The instrument depths were approximately 45 m for SODA-A, 42 m for SODA-B, and 27 m for SODA-C. To minimize the effects of mooring knock-down, the top float of each mooring was a DeepWater Buoyancy Stablemoor500, which are designed to remain level even during knockdown events (Harding et al., 2017). The maximum tilt deviation measured by any of the ADCPs was $\leq 2°$ from their resting position. A Seabird SBE-37 conductivity-temperature-depth sensor installed underneath the float ($\sim$1 m vertical offset from the ADCP) collected temperature and salinity measurements to compliment the temperature measurements made by the ADCP to calculate and correct the speed of sound (which is used to calculate altimeter distance).

The four slant beams of the ADCP measured velocity profiles, while the fifth vertical beam acted as an altimeter (fig. 1) and measured the distance to the surface (either the water surface or ice bottom). The vertical beam has a beam width of 2.9°, so for the deployment depths here, the width of the ensonified area was roughly 2.3 m for SODA-A, 2.1 m for SODA-B, and 1.4 m for SODA-C. The ADCPs operated with two concurrent sampling plans: "Average+Ice", and "Burst+Waves". For both modes, the

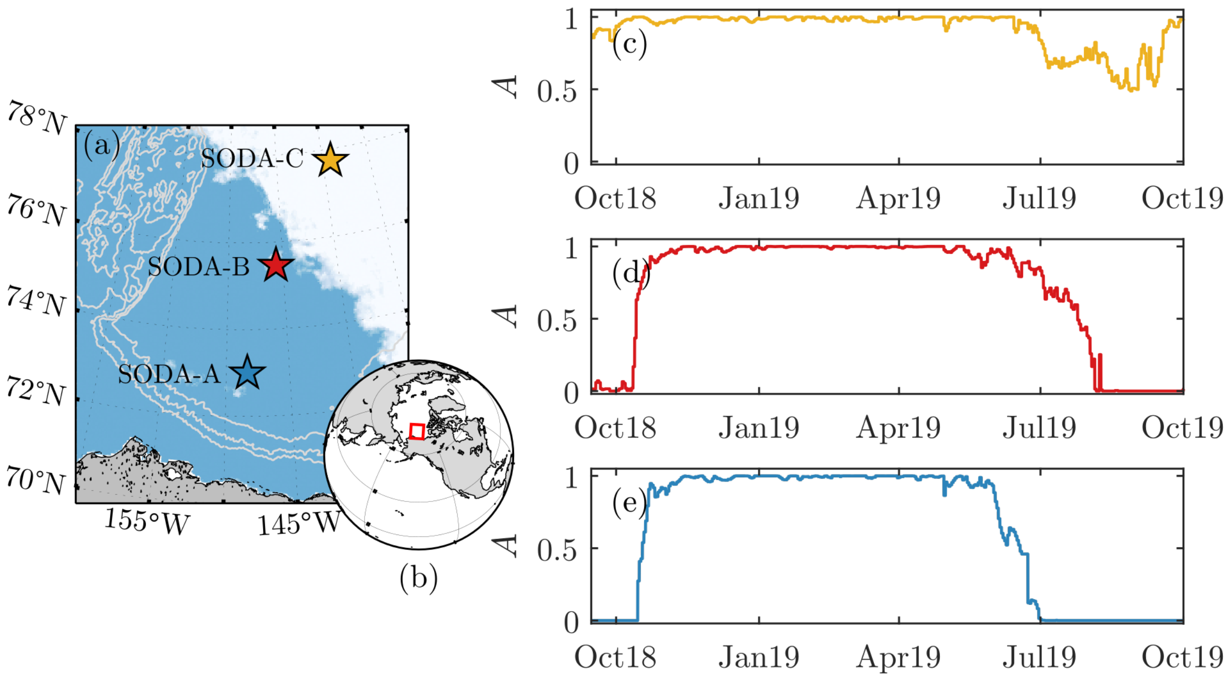

Figure 2: (a,b) Maps of (a) the Beaufort Sea showing the locations of the three moorings overlaid on sea ice concentration map from Sept. 18, 2018 (the 2018 sea ice minimum), with baythymetry shown by grey contours (contours are 1000-m isobaths); and (b) the location of (a). The ice concentration in (a) is from the Sea Ice Remote Sensing database at the University of Bremen (Spreen et al., 2008). (c–e) The annual cycle of sea ice concentration averaged over the mooring locations during the measurement period: (c) SODA-C, (d) SODA-B, and (e) SODA-A.

ice draft was derived from the difference between the water depth (determined by instrument pressure) and altimeter distance, after making corrections for ADCP tilt, speed of sound, and atmospheric pressure variations (e.g., Magnell et al., 2010; Krishfield et al., 2014).

During the Average+Ice sampling mode, the ADCP measured altimeter distance, water column velocity, and ice drift velocity (using the built-in ice-tracking mode). Measurements of each of these variables were provided every 10 min based on raw data collected in 1-min long ensembles at a sampling rate of 1 Hz (reported measurements are ensemble-medians after quality control processing of the raw data). The water velocities were measured in 2-m vertical range bins. At each time step, the velocity profiles were interpolated to find the horizontal velocity, $\boldsymbol{u}_o$, at a fixed reference depth, z_{ref}; here, $z_{ref} = 10\,\mathrm{m}$ to conform to the Tsamados et al. (2014) parameterization scheme. The 10-min sampled Average+Ice measurements of $\boldsymbol{u}_i$, $\boldsymbol{u}_o$, and d_i were bin-averaged in 1-h bins to match the atmospheric re-analysis measurements used (see below). The supporting information fig. S1 shows examples of the timeseries of each of the velocity components at SODA-B.

As indicated by its name, the Burst+Waves plan is designed for the measurement of surface gravity waves using altimeter measurements from the vertical beam. However, those altimeter measurements can also be used for measuring under-ice geometry (e.g., ice keels; Magnell et al., 2010). In Burst+Waves mode, the ADCPs measured "bursts" of data containing 2048 samples at a rate of 2 Hz, so each burst length was 1024 s (~ 17 min). These bursts were collected once every two hours. Because the Burst+Waves and Average+Ice measurement plans were concurrent, the ADCPs recorded two values of the ice drift speed during each burst. Using the mean of those two ice drift measurements, the sampling time for each burst was converted to an along-burst distance. Within each burst, ice draft data were despiked using a moving-median outlier criteria in 127-point windows (outliers are identified as points more than three scaled median absolute deviations from the median, and replaced with linearly interpolated values). Then, the ice draft from Burst+Waves sampling were used to characterize the ice geometry (see section 3.3).

We used atmospheric forcing from the European Center for Medium-Range Weather Forecasts (ECMWF) Reanalysis version 5 (ERA5; Hersbach et al., 2020). ERA5 provides hourly measurements at a 0.25°×0.25° grid resolution. A recent comparison with in situ measurements in the Eastern Arctic showed that of the six re-analysis products assessed, ERA5 provided the best representation of wind speed (which is the primary variable of interest here) during winter and spring, and second best (by a small margin) during summer (Graham et al., 2019). To generate a timeseries of atmospheric forcing at each mooring, grid points were averaged within a 30 km radius centred at each of the mooring locations (14–16 gridpoints per mooring). There is a degree of uncertainty in re-analysis wind measurements in the Arctic (particularly in the marginal ice zone; e.g., Brenner et al., 2020). Nonetheless, there is strong coherence between the re-analysis wind velocities and the in situ measured ice drift velocities (not shown) and associated high correlations between the two (correlation coefficients of $r = 0.69$, 0.75, and 0.63 for SODA-A, -B, and -C, respectively). The results presented are not overly sensitive to the choice of re-analysis product used.

3.2 Application of the force-balance approach

Following McPhee (1980; see also Randelhoff et al., 2014; Dewey, 2019), we use a force-balance approach (eq. 3) to calculate the ice-ocean stress, $\boldsymbol{\tau}_{io}$. Then the ice-ocean drag coefficient, C_{io}, is inferred from the quadratic drag law (eq. 1a).

The ice-ocean stress ($\boldsymbol{\tau}_{io}$) is calculated hourly with eq. (3) using data from the ADCP measurements and ERA5 re-analysis. The ice draft (d_i) and ice velocity ($\boldsymbol{u}_i$) are from the 1-hour-averaged ADCP measurements. The local acceleration ($\frac{\partial \boldsymbol{u}_i}{\partial t}$) is the numerical derivative of the 1-hour-averaged $\boldsymbol{u}_i$ values. The geostrophic velocity ($\boldsymbol{u}_g$) is estimated as the depth-averaged velocity between 5 m and 20 m (based on results by Armitage et al., 2017), and low-pass filtered with a 2-day cutoff (the result is insensitive to these choices for $\boldsymbol{u}_g$; see supplementary Text S2). The atmosphere-ice stress ($\boldsymbol{\tau}_{ai}$) is determined using the quadratic drag law (eq. 1b), with 10-m wind velocity and surface air density taken from ERA5 re-analysis and C_{ai} parameterized as a function of ice concentration (following ECMWF, 2019; see supporting information Text S2). In mixed ice-open water conditions, the atmosphere-ice stress, $\boldsymbol{\tau}_{ai}$, used in eq. (3) is distinct from the total atmospheric stress (eq. 4b). Because eq. (3) assumes that ice is in free drift, values for which the wind factor ($|\boldsymbol{u}_i|/|\boldsymbol{u}_a|$; determined hourly) was less than 2% were rejected (the so-called "2%-rule"). The use of wind factor as a filtering criteria implies an intermittency of internal ice stresses, which is consistent with Steele et al. (1997), who found that on short timescales the atmospheric stress input to the ice ($\boldsymbol{\tau}_{ai}$) was primarily balanced by only one of either the ocean-ice stress ($\boldsymbol{\tau}_{oi}$) or the internal ice stress. ($\nabla \cdot \boldsymbol{\sigma}$). The friction velocity ($\boldsymbol{u}_*$) is determined from $\boldsymbol{\tau}_{io}$ assuming a constant $\rho_o = 1025\,\mathrm{kg\,m^{-3}}$ (with the definition $\boldsymbol{\tau}_{io} = \rho_o \boldsymbol{u}_* |\boldsymbol{u}_*|$).

To calculate the ice-ocean drag coefficient, the record is split into windows. Within each window the quadratic drag law (eq. 1a) is applied by regressing hourly calculated values of $|\boldsymbol{u}_*|^2$ (as described above) with hourly measured $|\boldsymbol{u}_{rel}|^2$ (with $\boldsymbol{u}_o$ defined at a 10-m reference depth). Then the value of C_{io} is the slope of the regression line (fig. 3). Windows are chosen to be 7 days in length, which provides an average of 80 points in each window (after using the 2%-rule to exclude non-free-drift points). Based on average ice drift speeds, each window covers roughly 75 km of ice (though there is both spatial and temporal variability in the actual window size). While shorter window lengths can resolve some higher frequency variability at the expense of larger uncertainties, the overall seasonal patterns found here are not sensitive to the window length chosen. Regression was performed with a bisquare robust linear fitting algorithm and forced through the origin (Huber1981). This method iteratively reduced the weighting on outliers, which may occur, for example, from intermittent violation of the free-drift assumption. Performing regression within windows instead of calculating C_{io} on a point-by-point basis (as in Dewey, 2019) minimized the effects of noise and uncertainty (particularly for low values of $\boldsymbol{u}_{rel}$), which may have resulted from a combination of measurement noise, higher frequency temporal variations, or unaccounted stresses (e.g., internal ice stress). Calculated values of the drag coefficient were rejected if the uncertainty in C_{io} was $\geq 2.5 \times 10^{-3}$ (based on a t-test with 95% confidence interval; Bendat & Piersol, 1971). High uncertainties in C_{io} occurred most frequently in winter when many of the data were rejected due to free drift conditions not being met. Tests using non-linear fits of the form $|\boldsymbol{\tau}_{io}| \propto |\boldsymbol{u}_{rel}|^n$ (see section 5.1) did not produce better fits than the quadratic drag law with $n = 2$ (r^2 values from $n \neq 2$ fits were approximately equal to those with $n = 2$). Given the direct concurrent and collocated measurements of the ice and ocean velocities here, it was not necessary to exclude periods of small ice-ocean relative velocity, a condition often necessary when using satellite remote sensing to estimate ice velocities (e.g., in McPhee, 1980).

This method of drag calculation essentially asks what value of C_{io} would be required to reproduce the observed sea ice motion. In doing so, the method effectively integrates

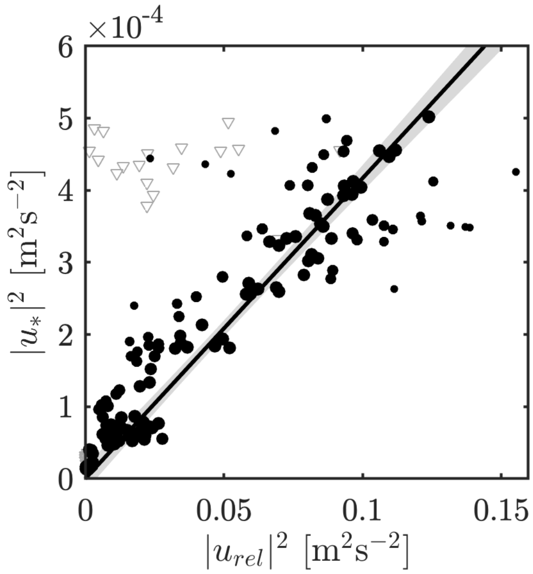

Figure 3: Example of quadratic-drag-law fit between hourly values of observed relative velocity ($|\boldsymbol{u}_{rel}|^2 = |\boldsymbol{u}_i - \boldsymbol{u}_o|^2$), and calculated friction velocity ($|\boldsymbol{u}_*|^2 = |\boldsymbol{\tau}_{io}|/\rho_o$) from the force-balance approach (eq. 3). Black points show values used in the fitting procedure, with point sizes an indicator of the relative weighting determined by the robust fitting method. Grey triangles show points rejected from the fit by the 2%-rule and demonstrate the utility of the wind factor to filter points that are not in free drift. The black line shows the regression line with 95% confidence interval shaded in grey. Data correspond to 1 week of measurements in November 2018 at SODA-A.

over both the temporal intermittency and the spatial heterogeneity of turbulent momentum fluxes across ice floes and thus provides bulk-average drag coefficient values. These resulting drag coefficients are appropriate for comparison to model parameterizations as the goal of those parameterizations is to provide a bulk coefficient for use within a model grid cell.

Because there is no physical basis to expect that the relationship between total ocean stress, $\boldsymbol{\tau}_{ocn}$, and wind speed should follow the quadratic drag law, so the linear fitting procedure use to calculate C_{io} can't be similarly applied to find C_{equiv}. Instead, C_{equiv} is computed on a point-by-point (hourly) basis using eq. (6), with $\boldsymbol{\tau}_{ocn}$ given by eq. (4a) and with A from ERA5. For points defined as being in free-drift (based on the 2%-rule), the ice-ocean stress, $\boldsymbol{\tau}_{io}$ used in eq. (4a) is the same as described above (eq. 3). The analysis was extended beyond free-drift periods by calculating $\boldsymbol{\tau}_{io}$ for those times using eq. (1a) and values of C_{io} from the regression procedure, interpolated to points with a wind factor $< 2\%$.

3.3 Ice geometry

During periods of ice cover, the ADCP Burst+Waves sampling provided one dimensional (along-drift) tracking of the under-ice geometry (fig. 4a). We use these to quantify the geometric characteristics used in the parameterization schemes in section 2. Importantly, the fixed mooring platforms allow for sampling across a broad range of different ice conditions as they evolve over the annual cycle. Ice-covered conditions were identified based on the relative partitioning of spectral energy in low or high frequency bands for each burst (e.g., Shcherbina et al., 2016; Kirillov et al., 2020): spectra from open water bursts have energy concentrated at higher frequencies due to the presence of surface gravity waves, while spectra from ice bursts are predominantly “red”. Here, we use a frequency cutoff of 0.1 Hz to distinguish high- and low-frequency bands, and identify ice-covered conditions when the ratio of high-to-low frequency variance is less than 5. Then, open-water bursts provide a secondary empirical correction to ice draft to account for water-column sound-speed variations (e.g., due to shallow stratification; Kirillov et al., 2020). These corrections were small, and primarily applied to marginal ice covered periods.

For each ice-covered burst we quantified the draft of level ice, the extent and number of leads, and the number and size of keels (fig. 4b). Prior to classification, bursts were smoothed with a moving-average filter using a centered window with a width of 2 m (because of variability in ice drift speed, the number of points in each window varies from burst to burst). Bursts frequently contained apparent leads, identified as all points in a burst with a measured draft below a tolerance level (taken as 0.15 m to account for instrument noise and uncertainty associated with both atmospheric pressure variations and sound speed). Strictly, this procedure is unable to differentiate between open-water leads and refrozen leads containing thin ice, but from the perspective of the drag parameterizations (section 2), both scenarios are dynamically equivalent in that they both contribute to the floe edge form drag. Within each burst, level ice was defined by a local gradient less than 0.025 (equivalent to the process in Wadhams & Horne, 1980) and a draft of less than 3 m (roughly the limit of thermodynamic growth; [CITE]). The level ice draft for

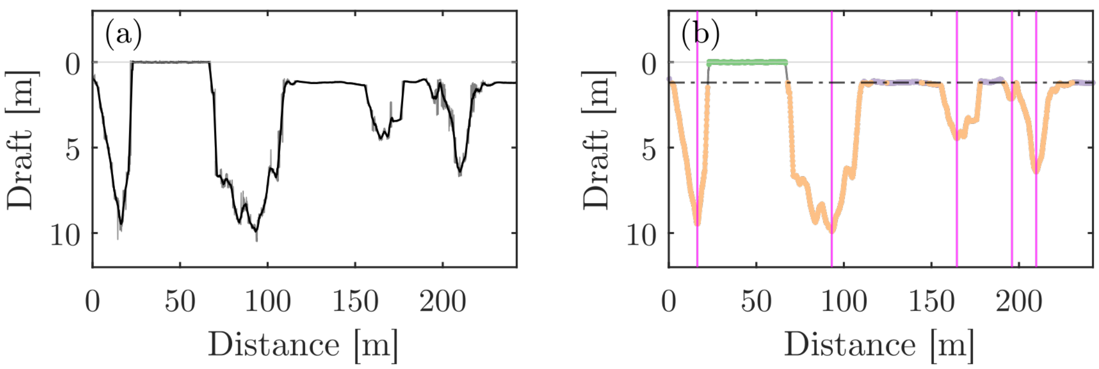

Figure 4: Example of ice draft from burst measurements: (a) Raw (thin grey line) and smoothed (black line) ice draft during a single burst (∼17 min) in April 2019 at SODA-A. (b) The burst from (a) classified to show leads (green line), level ice (purple), and ridged ice (orange), with vertical magenta lines showing unique keels (based on Rayleigh criterion), and black dashed-dotted line showing the level ice draft classified for that burst.

each burst was then taken as the median draft of all ice identified as level within the burst. In cases where no level ice was identified (i.e., the entire burst measured ridged ice), a level ice draft was found by interpolating across adjacent bursts. Keels identification followed Martin (2007), using a Rayleigh criterion to define unique keels (see also Williams et al., 1975; Wadhams & Horne, 1980; Wadhams & Davy, 1986) with a minimum keel depth cutoff of 0.5 m relative to the level ice draft for that burst. Relative keel depths at each of the moorings closely followed exponential probability distributions (not shown), which is in line with previous literature (e.g., Wadhams & Horne, 1980; Wadhams & Davy, 1986), and a total of 14 694 individual keels were identified throughout the full study period (6282, 4305, and 4107 at SODA-A, -B, and -C, respectively). The maximum relative keel depth measured at any of the moorings through the full deployment was 11.4 m at SODA-B. Keel sizes across the three moorings were fairly similar.

The parameterized ice-ocean drag is based on statistical descriptions of the ice geometry (see section 2). Statistics were accumulated over one week periods to be consistent with the windowing procedure for the ice-ocean drag (section 3.2). The keel depth (h_k) and level ice draft (d_{lvl}) are simply averages of individual measurements taken for all bursts in each window. The average keel spacing (ℓ_k) was taken as the total distance measured by all bursts in a given window (both ice and open water) divided by the total number of keels counted during that window. Except for some bursts in the marginal ice zone, floe chord lengths are typically longer than the distance measured by an individual burst. To estimate an average floe length (ℓ_f) the total measured ice-covered distance for a given window was divided by the number of leads counted in that window. Similarly, the average lead length (ℓ_l) was the total open water distance divided by the number of leads. These definitions for ℓ_k and ℓ_f are consistent with their inclusion in parameterizations (Lu et al., 2011; Tsamados et al., 2014). A local average daily ice concentration, (A) was also calculated using burst data as a ratio of the total measured ice-covered distance to the total distance measured by all bursts (ice and open water). Using A, the average lead length can be written as $\ell_l = \ell_f(1-A)/A$ for one-dimensional measurements (Lu et al., 2011). The values ℓ_f and ℓ_l are only defined for ice concentration less than 100%. The measurements show seasonal signals in all of the measured geometry statistics at all moorings (fig. 5). Despite both d_{lvl} and ℓ_f decreasing in the summer/fall (figs. 5a and 5c), the much wider range of variation of ℓ_f (over roughly 3 order of magnitude) compared to d_{lvl} results in floe aspect ratios (d_{lvl}/ℓ_f) that are elevated in the fall (fig. 5e). The relative keel depths and spacing ($h_{k\mathrm{rel}}$ and ℓ_k) appear to have some negative correlation (cf., figs. 5b and 5d), so that both signals contribute to the minimum ridging intensity (h_k/ℓ_k) in the summer/fall (fig. 5f).

3.4 Implementing model parameterization schemes

Four different variations of ice-ocean drag parametrizations were tested. These are summarized in table 2. In the first two variations (labelled L11 and T14(I), respectively), direct measurements of the sea ice geometry (section 3.3) were used to test the parameterization schemes proposed by Lu et al. (2011) and Tsamados et al. (2014) (section 2.1) using default parameter values in each scheme. Another variation tested an alternative version of the Tsamados et al. (2014) scheme, labelled T14(II), which uses slightly modified geometry definitions and coefficient values. Finally, the T14(III) variation tested a combination of both physics and ice geometry parametrization from Tsamados et al. (2014).

The T14(II) scheme is a modification of the T14(I) scheme. It still uses the direct measurements of sea ice geometry, but uses the relative definitions of keel depth and reference depth (see section 2.1). Additionally, in T14(II), some of the parameters have been changed from their default values. The local skin drag coefficient (c_s) is replaced with

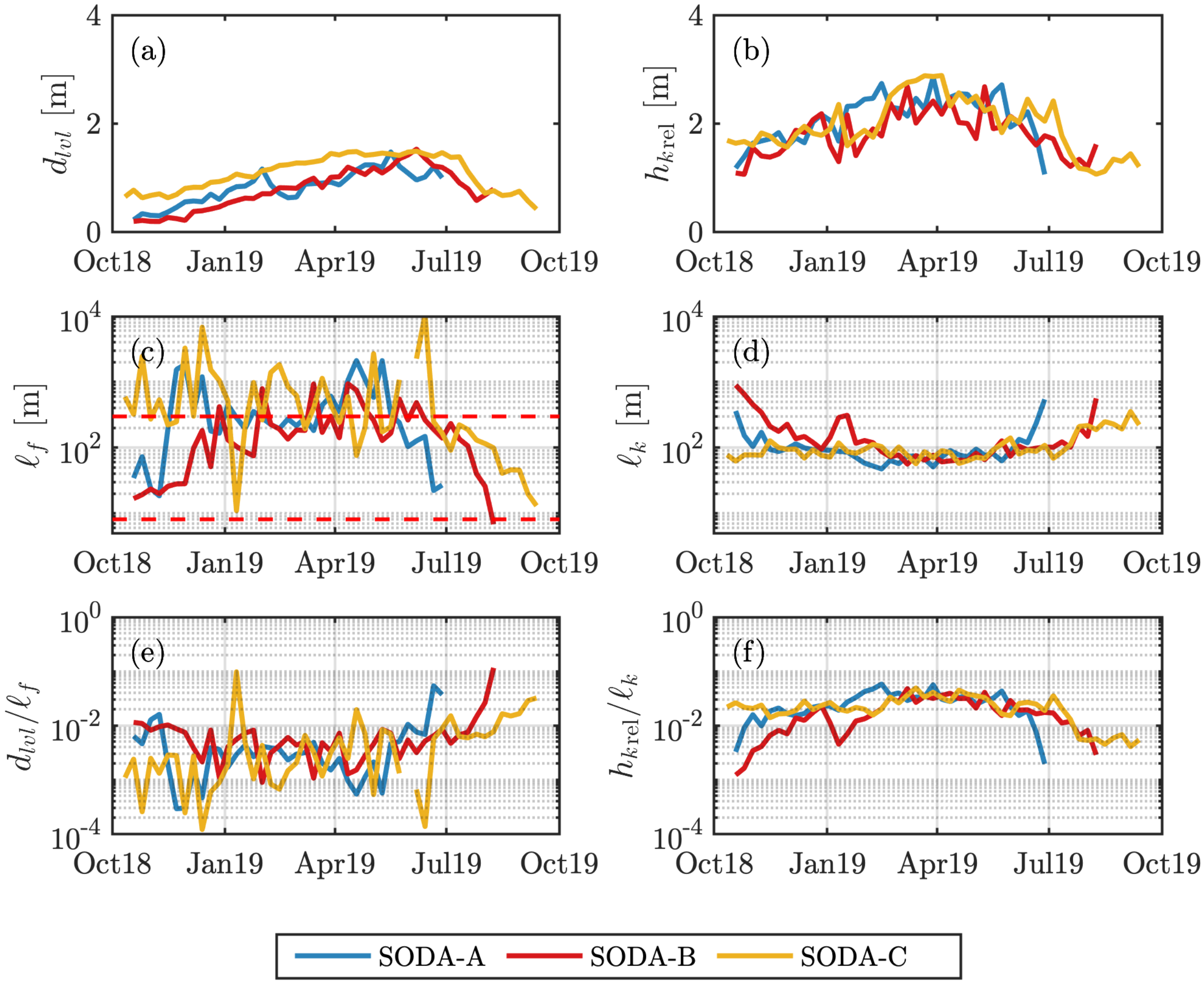

Figure 5: Weekly statistics of sea ice geometry for each mooring: (a) mean level ice draft; (b) mean relative keel height; (c) mean floe length; (d) mean keel spacing (e) aspect ratio (d_{lvl}/ℓ_f); and (f) ridging intensity (h_k/ℓ_k). Horizontal dashed red lines in (c) show the maximum and minimum extents of the parametrized floe length (eq. 13).

Table 2: Summary of parameters and functions used in the parameterization schemes tested.

	L11	T14(I)	T14(II)	T14(III)
c_f	1	1	$0.3^{\dagger}$	1
c_k	$1/\pi$	0.2	$0.4^{\dagger}$	0.2
c_s	2×10^{-3}	2×10^{-3}	eq. $(11)^{\ddagger}$	2×10^{-3}
z_{0i}	n/a	5×10^{-4} m	1×10^{-3} m	5×10^{-4} m
z_{0w}	n/a	3.27×10^{-4} m	3.27×10^{-4} m	3.27×10^{-4} m
m_w	10	10	10	10
s_l	n/a	0.18	0.18	0.18
S_c	eq. (9b)	eq. (9a)	eq. (9a)	eq. (9a)
P_0	n/a	eq. (10)	eq. $(10)^{\ddagger}$	eq. (10)
h_k	$h_{k\mathrm{rel}}$	$h_{k\mathrm{tot}}$	$h_{k\mathrm{rel}}$	eq. (12a)
ℓ_k	meas.	meas.	meas.	eq. (12b)
ℓ_f	meas.	meas.	meas.	eq. (13)

†parameters adjusted based on best fit to observations;
‡using a relative reference depth ($z_{\mathrm{ref}} - d_{lvl}$);
n/a: not applicable;
meas.: measured (see section 3.3)

eq. (11) and the roughness length associated with level ice, z_{0i} is replaced with a value of 1×10^{-3} m, which is reflective of observations of ice with no significant morphology (McPhee et al., 1999; McPhee, 2002). With this z_{0i} and a 10-m reference depth, the value of c_s calculated for a 1-m ice draft is 2×10^{-3}, which is the same as in T14(I); however, the use of eq. (11) allows c_s to vary slightly through the year as the ice draft changes seasonally, and gives it an explicit dependence on z_{ref}. By using this formulation c_s is no longer a free parameter. Finally, the local form drag coefficients (c_f, c_k) have been replaced with values that provide the closest fit between parameterized and observed drag coefficient values when considered across all moorings. Note that this does not reflect a full optimization tuning of all of the available parameters (discussed further in section 4.2).

As the ADCP measurements provide direct observations of ice geometry (section 3.3), the parametrization of ice geometry (section 2.2) is not necessary in order to implement eq. (8) in L11, T14(I), and T14(II). Instead, this allows us to separately test the physics parameterization (section 2.1) and the geometry parameterization (section 2.2). To do so, a final variation (T14(III)) is tested that uses the default parameter values from Tsamados et al. (2014) but instead of using the direct measurements of sea ice geometry, geometry statistics are estimated using bulk measurements and eqs. (12) and (13).

Application of eq. (12) using ADCP measurements provides some challenges. The ice volume (v_{rdg}) and areas (a_{rdg}, a_i) in eq. (12) are fundamentally defined over a two dimensional area (i.e., within a model gridcell), but the ADCP draft measurements are one dimensional (along-drift). To adapt our measurements to apply eq. (12), we calculate v_{rdg}, a_{rdg}, and a_i on a per-unit-width basis. However, the relative angles between the keel orientations and the direction of sampling (which is unknown) will cause an overestimate of the area or volume of the feature unless measurements are made perpendicular to the keels. Fortunately, this mismatch creates an equal bias for both volume and area calculations, so the ratio v_{rdg}/a_{rdg} in eq. (12a) is not impacted. However, due to crossing angle mismatch, extra care must be taken when calculating and interpreting ℓ_f from eq. (12b). If both keels and leads are linear features whose orientations follow the same statistical distributions then the ratio a_i/a_{rdg} measured with along-drift data will approximate the true (two-dimensional) value if averaged over a sufficiently large sample of keels and leads. However, in full ice cover leads are relatively scarce while in the marginal ice zone it may not be appropriate to consider leads to be linear features. It is unclear whether one-dimensional sampling of a_i will introduce any mean bias. For a uniformly distributed keel orientation, one-dimensional sampling will lead to a mean overestimate of a_{rdg} by a factor of $\pi/2$. On that basis a_{rdg} are multiplied by a $2/\pi$ correction factor when applying eq. (12b).

4 Results

4.1 Seasonal and spatial variation of ice-ocean drag

For all three moorings, the force-balance approach provided estimates for the ice-ocean drag coefficient, C_{io}, throughout the full annual cycle (fig. 6) even despite some winter data gaps (due to higher internal stresses). These estimated values of the ice-ocean drag coefficient exhibit both spatial and seasonal variations.

Drag coefficients measured at SODA-A and SODA-B (the two southern moorings; fig. 2a) show a similar seasonal behaviour. For both, the drag coefficients start at low values (C_{io} ~2×10^{-3} to 3×10^{-3}), and steadily increase through the winter to a maximum in spring (Apr.–May) before declining (figs. 6b and 6c). The decrease of C_{io} is more gradual at SODA-B than SODA-A, and summertime minimum values at SODA-A are lower than at SODA-B (cf., figs. 6b and 6c). The timing of the shift from increasing to decreasing C_{io} at these two moorings is roughly coincident with the change from net surface cooling to net surface heating in the atmospheric re-analysis data, which occurred in Apr.–May.

In contrast, the record at SODA-C begins with an elevated drag coefficient ($C_{io} \sim 6 \times 10^{-3}$) which remains roughly constant from fall through spring (fig. 6a). After the shift to net atmospheric surface heating in Apr.–May, there may be a slight decline in C_{io}, but values are still elevated for some months, until there is a sharp drop in early to mid-July. This sudden drop in ice-ocean drag is associated with a similar sharp decline in both floe sizes (fig. 5c) and ridging intensity (fig. 5f), suggesting a dramatic ice breakup and melting event occurred.

At all three moorings, drag coefficient values from mid-winter to spring are similar to each other, and fluctuate near or above the canonical value of $C_{io} = 5.5 \times 10^{-3}$. However, differences between the moorings in fall and summer imply large-scale spatial gradients in the ice-ocean drag coefficient across the Beaufort Sea. Section 4.3 discusses morphological drivers of the observed seasonality in greater depth.

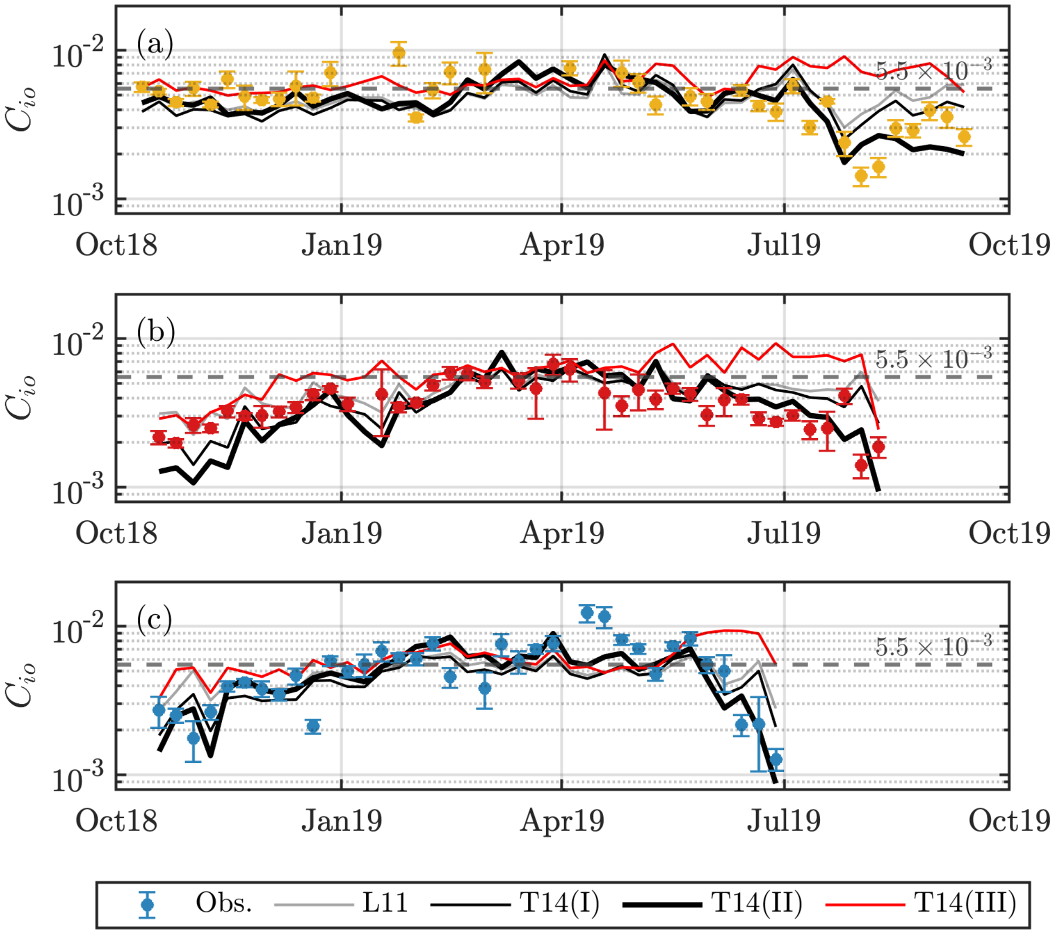

Figure 6: Ice-ocean drag coefficients from north-to-south: (a) SODA-C, (b) SODA-B, and (c) SODA-A. In each panel, points with error-bars (coloured by moorings per fig. 2a) show the values of C_{io} calculated with the force-balance approach (labelled "Obs."), while lines correspond to the different variations of parameterization schemes (table 2), as indicated by the legend. Error bars show 95%-confidence interval bounds from the linear fitting procedure. The horizontal grey dashed line shows the value of $C_{io} = 5.5 \times 10^{-3}$ for comparison.

4.2 Evaluation of parametrization schemes

Ice-ocean drag coefficients calculated with the all of the tested parameterization schemes (table 2) show values and temporal variability that broadly match the values observed with the force-balance approach (fig. 6). This agreement indicates that variability of ice-ocean drag can be primarily explained by seasonal changes in the ice morphology and the associated skin/form drag contributions. Despite general success, some versions of the parametrization schemes are better performing; in particular, the T14(III) scheme diverges significantly from the observations in the latter half of the record, and even reaches a maximum C_{io} in summer/fall when the observations show a minimum. Figure 7 shows direct comparisons of the observed and parametrized values for each of the four test schemes. There is good agreement between the observed drag coefficients and those predicted by both L11 and T14(I) when C_{io} are low ($\lesssim 5 \times 10^{-3}$); for higher values of C_{io} ($\gtrsim 5 \times 10^{-3}$), there is a roll-off of the modelled values (figs. 7a and 7b). Values from T14(II) follow the one-to-one line across the full range of C_{io} (fig. 7c), while those from T14(III) are mostly above the one-to-one line and don't present any recognizable correlation with force-balance observations. A few notable outliers exist that aren't described by any of the model schemes (e.g., high observed values of drag in mid-April at SODA-A; fig. 6a), potentially suggesting other sources of drag (e.g., internal wave drag) that can't be explained by ice geometry variations alone; however, these points are fairly limited.

These statements are corroborated by quantitative assessments of model performance across all moorings (table 3). Values from both L11 and T14(I) have weak correlations with observations ($r^2 = 0.13$ and 0.22, respectively). T14(I) has a slightly negative normalized bias (NBI; -012), while L11 is approximately unbiased. The T14(II) scheme has the best correlation of the four tests ($r^2 = 0.46$), the lowest normalized root-mean-squared error (NRMSE; 0.31), though it also has a slightly negative normalized bias (-0.09). The T14(III) scheme is biased high (NBI of 0.31), has high NRMSE (0.57), and is uncorrelated with observations. Tests in which the observed drag coefficients and geometry statistics were determined using different window lengths (ranging between 1 d and 14 d) all produce similar correlations as the 7-d windows presented (not shown), giving confidence that the parameterization schemes are appropriate over a wide range of scales.

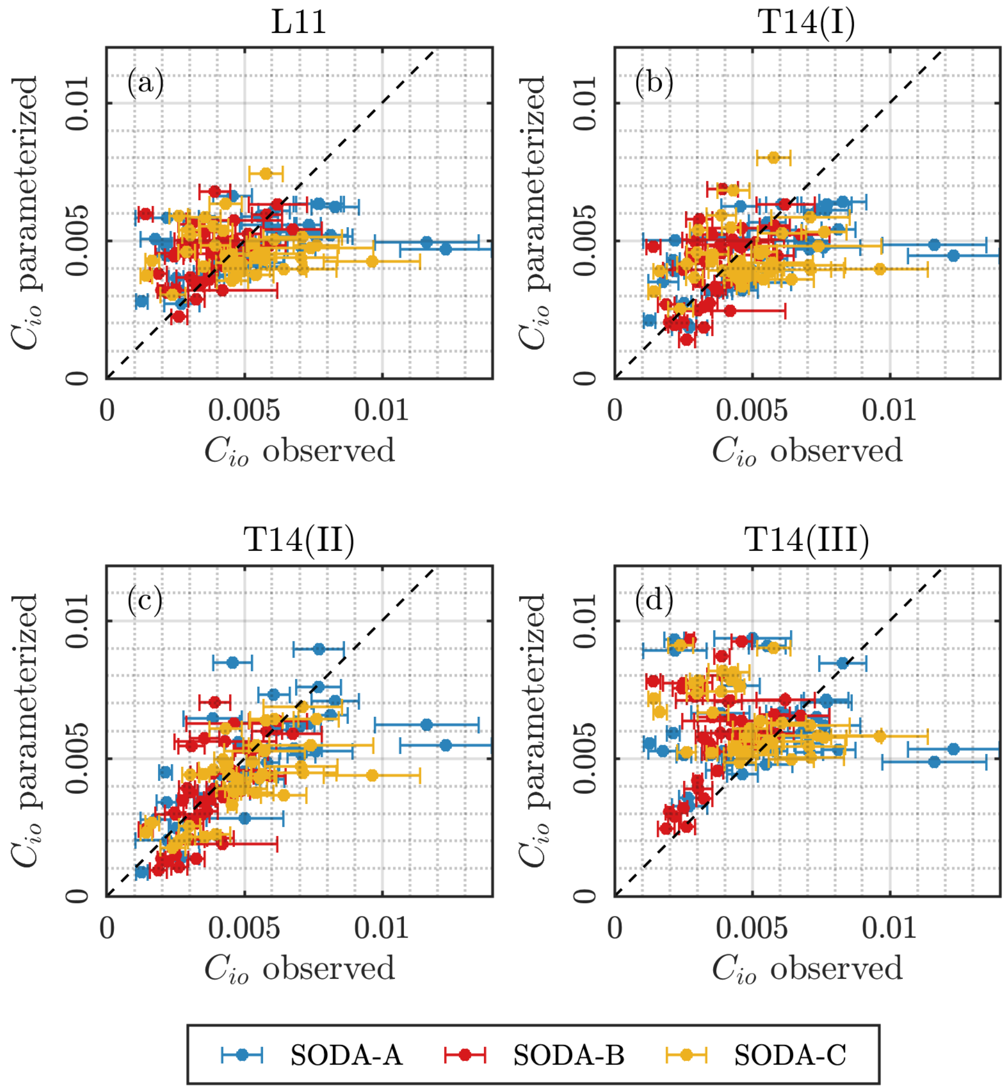

Figure 7: A comparison between the ice-ocean drag coefficients determined using the force-balance approach ("observed"), and using the different variations of geometry-based parameterization: (a) L11, (b) T14(I), (c) T14(II), and (d) T14(III). In each panel, the black dashed line shows the one-to-one slope, and the points are coloured by mooring according the legend.

Table 3: Summary of fit statistics of ice-ocean drag coefficients determined using the force-balance approach and using the different variations of geometry-based parameterization. (NRSME = normalized root mean square error; NBI = normalized bias)

Scheme	r^2	NRMSE	NBI
L11	0.13	0.37	-0.00
T14(I)	0.22	0.36	-0.08
T14(II)	0.46	0.31	-0.09
T14(III)	0.00	0.57	0.31

The parameterization schemes tested include a number of constants that could be used to tune the modelled drag coefficients (c_f, c_k, c_s, s_l, z_{0w}, z_{0i}, m_w). While the T14(II) scheme modifies some parameters from default values (table 2), detailed optimization accounting for all free parameters is deliberately not performed here. This is choice is primarily driven by the fact that the tests here do not account for all of the physical processes that modify the ice-ocean drag coefficient. In particular, the parameterization schemes only model the neutral drag coefficient and do not account for variations due to buoyancy (which should be included as a correction term; e.g. Lüpkes & Gryanik, 2015), whereas the observed values of C_{io} reflect the total drag, including non-neutral effects and stratification. Additionally, drag due to internal wave radiation is thought to be important in some oceanographic conditions (McPhee & Kantha, 1989; Pite et al., 1995) but is not included. Finally, the forms of the functions P_0 (eq. 10) and c_s (eq. 11) are based on an assumed velocity profile that may not be suitable through the full reference depth; the logarithmic boundary layer at the ice-ocean interface is thought to be only $\sim$2 m thick (e.g. McPhee, 2002; Shaw et al., 2008; Randelhoff et al., 2014; Cole et al., 2017), which is much shallower than the 10-m reference depth used. The generally close match between parameterized values of C_{io} (with T14(II)) and those determined through the force balance suggest that these effects may be small, but they should still be considered before a more thorough optimization of free parameters is performed.

4.3 Partitioning of drag components and predictions of ice geometry

Parameterized ice-ocean drag coefficients are built up from three components: form drag on floe edges (eq. 8a), form drag on keels (eq. 8b), and skin drag (eq. 8c). Insofar as the ice-ocean drag coefficient is driven by ice morphology, examination of the partitioning of drag components allows us to better understand the impact of those morphological variations. In all four of the parametrization schemes tested, the ice-ocean drag coefficient in the winter is largely driven by form drag on ice keels (C_k). Skin drag (C_s) is generally much smaller, and does not show significant seasonal variation, and floe edge drag (C_f) becomes more important in the summer as the ice begins to melt and break apart into smaller floes. This general pattern qualitatively matches results from sea ice models (Tsamados et al., 2014; Martin et al., 2016), but details vary from those model results.

In the T14(II) scheme (which provides the best match with observations), the seasonality of C_{io} observed in fig. 6 is driven by seasonal growth and melt of ice keels, as seen by variation in C_k (figs. 8a to 8c). At the southern moorings (SODA-A, -B), which start the timeseries in open water, there is initially only small contribution from C_k and most of the drag is due to C_s. As the number and size of keels grow through the year (fig. 5), so too does the contribution from C_k (figs. 8b and 8c). At SODA-C, the timeseries begins in ice cover with established ridging, and C_k is the main component of C_{io} from the onset (fig. 8a). All three moorings have some small contributions to floe edge drag throughout the full year due to the presence of (potentially refrozen) leads. Following the onset of melting conditions, an increase in floe edge drag accompanies the decline of keel drag at all locations; however, the increased floe edge drag is not enough to compensate for the lack of keels at any of the moorings (figs. 8a to 8c). This contrasts the modelling results from Tsamados et al. (2014) and Martin et al. (2016), which show that floe edge drag is substantial during summer/fall. While not the main focus here, it is also noteworthy that keel decline varied between the three moorings: at both the southernmost mooring (SODA-A) and northernmost mooring (SODA-C), there was a fairly rapid drop in C_k over the period of approximately 2 weeks in late June and early July, respectively, due to both decreased size and number of keels (figs. 5b and 5d); at SODA-B, the decrease in C_k was more gradual. Note that at SODA-A and -B, where there was a strong seasonality in keel drag, growth of C_k proceeded at a much slower rate than ice cover growth; at both moorings, ice concentration was close to 100% by early

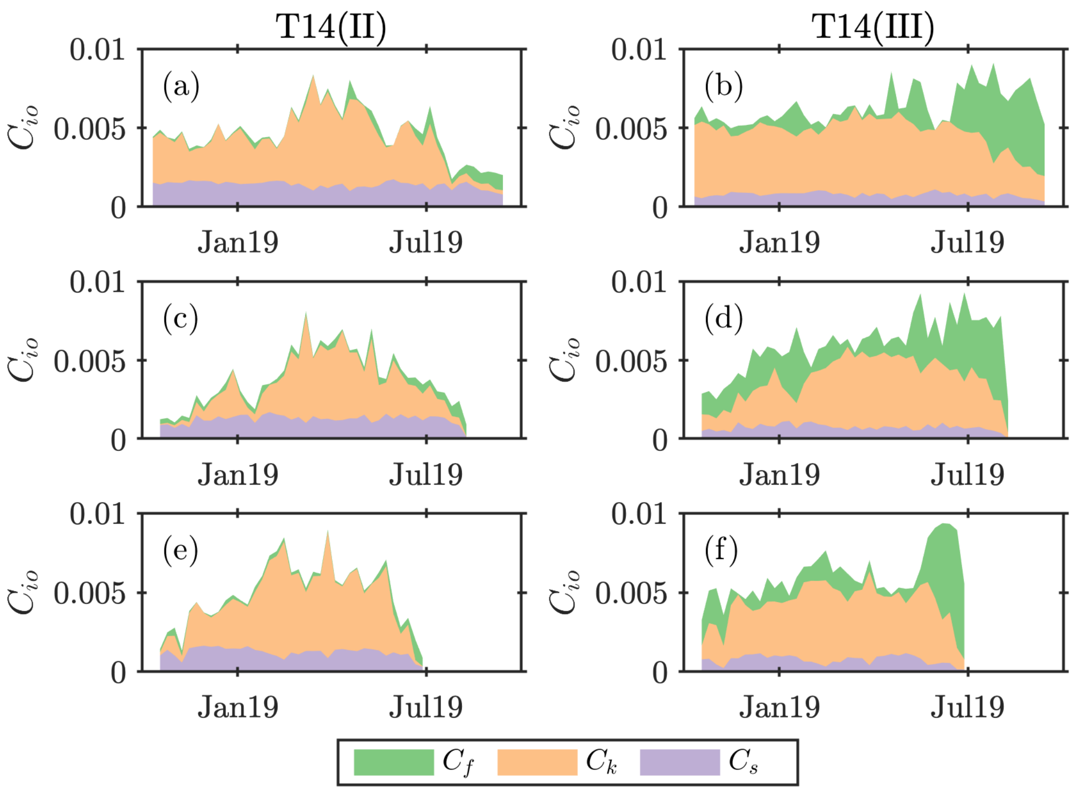

Figure 8: Stacked contributions to the ice-ocean drag coefficient C_{io} from form drag on floe edges (C_f), form drag on keels (C_k), and skin drag (C_s) calculated using (a-c) the T14(II) scheme, and (d-f) the T14(III) scheme (see table 2) for (a,d) SODA-C, (b,e) SODA-B, and (c,f) SODA-A.

November (figs. 2c to 2e), while C_k remained relatively low through January. As such, it is unlikely that ice concentration based drag parameterizations (such as are suggested for atmospheric drag; e.g., Andreas, Horst, et al., 2010) would ever be able to sufficiently capture observed seasonal variations in C_{io}.

The drag partition from the T14(III) scheme (figs. 8d to 8f) differs from the results of the T14(II) scheme. While keel drag (C_k) is still the dominant contribution during winter, its seasonality is somewhat muted compared to T14(II) (compare C_k in figs. 8a to 8c with figs. 8d to 8f). More striking are the differences in floe edge drag: C_f is much higher in the T14(III) scheme at all moorings and times of the year, and in summer/fall the increase in C_f outpaces the associated decrease in C_k. As a result, the T14(III) scheme has the largest value of C_{io} in summer/fall, which conforms to previous model results

(Tsamados et al., 2014; Martin et al., 2016). While these differences can be partly attributed to the differences in "local" drag coefficients between the two schemes (c_f and c_k, see table 2), the main difference arises from the fact that the T14(III) scheme does not use direct measurements of the sea ice geometry, and instead relies on parametrized geometry statistics (section 2.2).

Differences in C_f between T14(II) and T14(III) depend mainly on the floe aspect ratio, d_{lvl}/ℓ_f, while differences in C_k depend on the ridging intensity, h_k/ℓ_k. As shown in figs. 9a and 9c, neither of these ratios is well predicted by the parametrizations of ice geometry eqs. (12) and (13), with parametrizations overestimating the results in both cases. For the highest values of ridging intensity ($h_k/\ell_k \gtrsim 5 \times 10^{-2}$) predicted values fall near the one-to-one line but deviate substantially as observed values decrease (fig. 9a). As such, the overall magnitude of C_k values is not strongly modified by the over-prediction of ridging intensity, but the decreased range of variability of modelled values is responsible for the muted seasonality of C_k seen in the T14(III) scheme. Considering the separate roles of h_k and ℓ_k in setting this ratio, the predictions of each individual variable have as much (or more) variability as observations (fig. 9b), but there is an apparent compensating effect between the two quantities. Predicted values of h_k and ℓ_k vary roughly along lines of constant h_k/ℓ_k, while observations vary primarily across lines of h_k/ℓ_k.

The elevated levels of C_f seen in the T14(III) test result from parameterized values of the aspect ratio, d_{lvl}/ℓ_f, being much greater than observations across nearly the full range of values (fig. 9c), with a median factor of $\sim$4 times higher than the observed values. Differences between the observed and predicted aspect ratio are driven solely by differences in ℓ_f (d_{lvl} is not parameterized). The relationship between floe lengths and ice concentration used in eq. (13) to predict ℓ_f is an empirical result derived from a set of aerial photos of ice in the marginal ice zone in the Fram Strait (Lüpkes et al., 2012). However, a wide variety of factors set the size and density of floes (Roach et al., 2018) and so it is unlikely that such empirical relationships would be valid in different Arctic regions and all times of year. The mismatch in the seasonality of C_{io} between observations and values predicted with the T14(III) parameterization arise mainly from this overestimate of aspect ratio. In ad hoc tests using different combinations of parameters ($\ell_{f,max}$, b_2, and A_*) in eq. (13), there are no combinations that reduce C_f enough to reverse the seasonal mismatch.

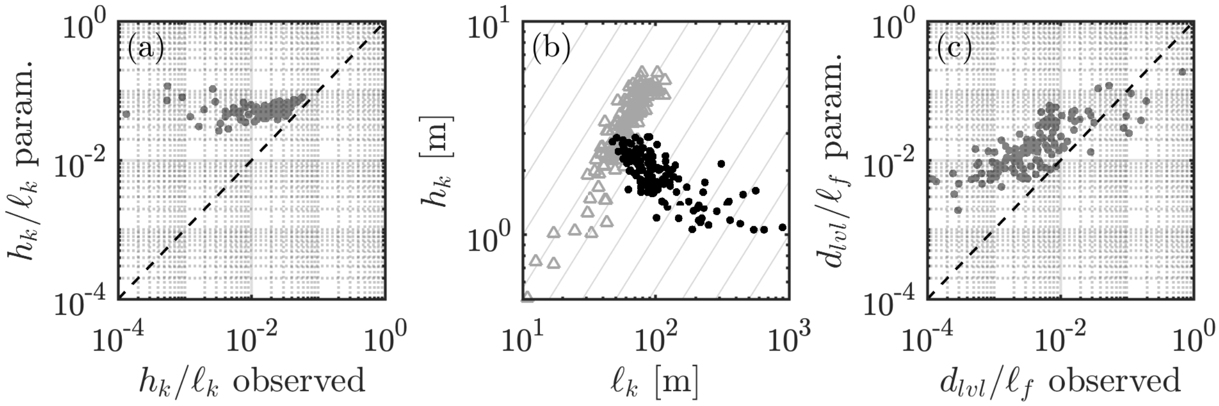

Figure 9: A comparison of observed and parameterized sea ice geometry statistics: (a) Observed versus parameterized ridging intensity (h_k/ℓ_k) with daily values measured at all moorings; the black dashed line shows the one-to-one slope. (b) Weekly-averaged values of ridge spacing (ℓ_k) versus keep depth (h_k) from observations (black points) and parameterizations (grey triangles). Grey contours correspond to lines of constant h_k/ℓ_k. Observed values of h_k in (a) and (b) are relative keel depth ($h_{k\mathrm{rel}}$). (c) As per (a) but for aspect ratio (d_{lvl}/ℓ_f).

5 Discussion

5.1 Comparison with previous drag observations

The range of values reported for the ice-ocean drag coefficient are consistent with previous observations. Shirasawa and Ingram (1991) and Lu et al. (2011) collated observations of the ice-ocean drag coefficient from a wide set of historical studies (publication dates from 1970 to 1997). These studies indicate a broad range of measured values with extremes from as low as 0.13×10^{-3} (under land-fast ice in Hudson's bay; Shirasawa et al., 1989) to the highest value of 47×10^{-3} (indirectly estimated based on fitting log-layer profiles to velocity measurements; Johannessen, 1970). The bulk of the studies summarized suggest drag coefficient values range from roughly 1×10^{-3} to 20×10^{-3}. More modern studies based either on direct measurements (Shaw et al., 2008; Randelhoff et al., 2014; Cole et al., 2014, 2017) or force-balance approaches (Randelhoff et al., 2014; T. W. Kim et al., 2017; Dewey, 2019; Heorton et al., 2019) provide similar limits. This study finds drag coefficient values from 1.3×10^{-3} to 12.3×10^{-3}, which fall well within the conventional bounds, and the mean and median values are close to, but slightly

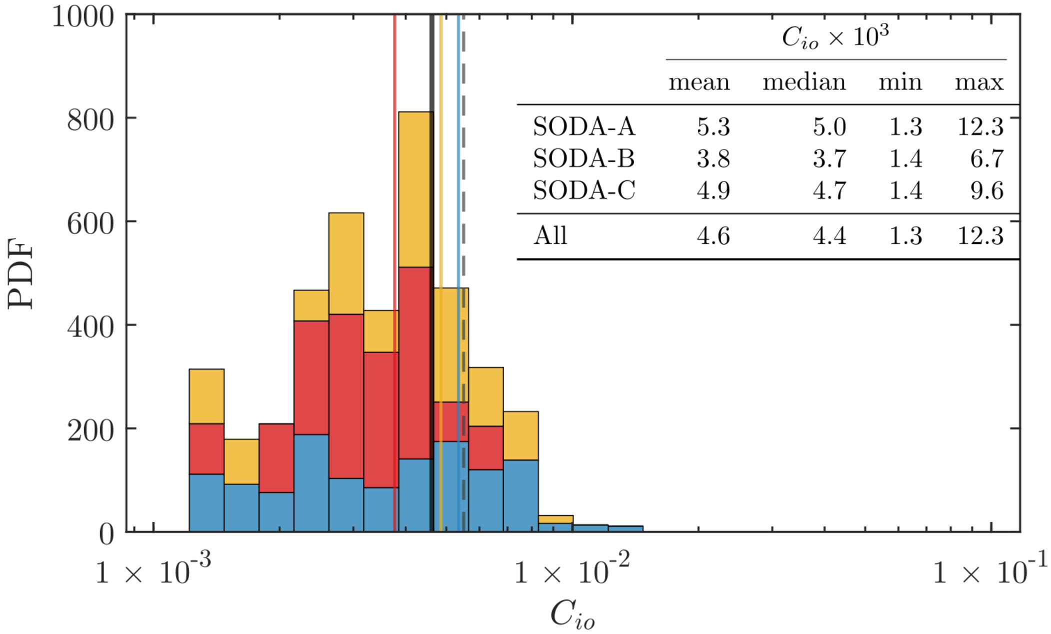

Figure 10: Stacked histograms showing the probability distribution function (PDF) of the ice-ocean drag coefficient values calculated at each of the three moorings (coloured by mooring according to fig. 2a). Coloured vertical lines show the annual mean value of C_{io} for each mooring, and the vertical black line shows the overall mean. The vertical grey dashed line shows the value of $C_{io} = 5.5 \times 10^{-3}$ for comparison.

below, the canonical drag coefficient value of 5.5×10^{-3} (fig. 10). The overall mean value of 4.6×10^{-3} in these observations is very similar to the average ice-ocean drag coefficient of 4.7×10^{-3} found by Dewey (2019) for the Beaufort Sea.

Cole et al. (2017) present detailed analysis of surface momentum flux from four ice drift stations in the Beaufort Sea, each containing a cluster of autonomous instruments. The four clusters provide measurements spanning March to December 2014, nearly a full annual cycle. Their results show weekly median ice-ocean drag coefficients ranging from approximately 0.2×10^{-3} to 10×10^{-3}, with significant spatial and temporal variability (see their figure 12). Their measured values of C_{io} span a broader range than reported here, with minimum values an order-of-magnitude lower than ours (but similar maximum values). Nonetheless, there is good agreement with some of the qualitative behaviour exhibited by the ice cluster measurements. Namely, despite strong spatial variation in the values of C_{io}, all of the ice clusters showed consistent seasonal variations in ice-ocean drag, with minimum values at the time of ice minimum (Aug.–Sep.) and maximum values in spring (Apr.–Jun.). Dewey (2019) find a similar seasonal cycle based on a force-balance approach to calculate C_{io} from remote measurements in the Beaufort Sea over a 5-year period from 2011–2016: basin-wide average C_{io} show minimum values from Jul.–Oct. of each year. These patterns are in agreement with our observations which show minimum ice-ocean drag coefficient values in fall (fig. 6). In contrast, pan-Arctic averages of C_{io} from models incorporating a variable drag coefficient scheme (section 2.1) show the opposite behaviour (Tsamados et al., 2014; Martin et al., 2016). In those models, the maximum value of C_{io} occurs during the summer/fall season, driven by form drag on floe edges (eq. 8a). As described above (section 4.3), seasonality in modelled values of C_{io} may be a result of over predicted values of the floe aspect ratio, d_{lvl}/ℓ_f.

With a few exceptions, direct observational estimates of the ice-ocean drag coefficient are made using point measurements of turbulent fluxes. In comparison to the force-balance approach used here, C_{io} values derived from point measurements require far fewer assumptions about the ice dynamics (e.g., they are valid whether or not the ice is in free drift). However, these measurements are also inherently local and as such it is not clear how they scale to application across entire ice floes. For logistical reasons, measurements are typically made away from ice keels, so reported values of C_{io} may under-represent floe- or regional-average values (McPhee, 2012). Randelhoff et al. (2014) provide a direct comparison between a force-balance approach to calculate ice-ocean drag (the procedure used here) and in-situ measurements of turbulent fluxes. Their results showed that the force-balance approach produced ice-ocean stress estimates that were, on average, 3 times larger than direct measurements. They attribute the mismatch to unmeasured sources of drag (e.g., due to internal wave radiation; McPhee & Kantha, 1989), but it may also be due to non-local turbulence. Similarly, application of the force-balance approach to the ice cluster data from Cole et al. (2017) shows higher values of C_{io} and decreased temporal variability compared to local measurements (Heorton et al., 2019). While this may explain why the values of C_{io} observed here have a much higher minimum value than those by Cole et al. (2017), more work is needed to understand the inherent differences in between direct point measurements and force-balance measurements of ice-ocean drag.

In comparing values of C_{io} between different studies, it is important to consider the choice of reference depth used, which will impact the drag coefficient through depth variations of u_o. For example, repeating our analysis with a shallower reference depth of $z_{ref} = 6\,\mathrm{m}$ yields slightly higher values of C_{io}, with an overall average of 5.2×10^{-3} (compared to 4.6×10^{-3} for $z_{ref} = 10\,\mathrm{m}$). Typically, values of C_{io} are reported corresponding to either fixed reference depths near the ice bottom, thus in or near the logarithmic boundary layer, or they are reported using the underlying geostrophic current, $\boldsymbol{u}_g$, as a reference velocity (table 1 in Lu et al., 2011, lists reference depths used for a number of studies). Within the log-layer, $u_o \propto u_*$, so the application of the quadratic drag law is appropriate. However, beyond the logarithmic layer, the relationship between stress and velocity in the ice-ocean boundary layer is not expected to be quadratic (e.g. McPhee, 2008, and references therein). If $\boldsymbol{u}_g$ is used as a reference velocity, drag may be better described by Rossby Similarity Theory (Blackadar & Tennekes, 1968; McPhee, 2008), which accounts for the existence of an outer Ekman-like layer matched to an inner logarithmic layer (as has been observed in the ice-ocean boundary layer, e.g., Hunkins, 1966; McPhee, 1979). In this more general case, McPhee (1979, and others) find reasonable empirical agreement from an alternative power law form: $|\boldsymbol{\tau}_{io}| \propto |\boldsymbol{u}_i - \boldsymbol{u}_g|^n$ where $n < 2$ (e.g., Cole et al., 2017, find values of n ranging from 0.51 to 1.76). The use of a fixed reference depth of $z_{ref} = 10\,\mathrm{m}$ in the present study likely extends beyond the surface log-layer so the quadratic drag law is not strictly applicable. Nonetheless, tested parameterizations that assume a law-of-the-wall velocity profile (T14(I), T14(II)) produce reasonable results (figs. 6 and 7). Furthermore, the relationship between stress and relative velocity seems to be well described by the quadratic drag law (fig. 3). This suggests a “fuzzy” transition between the inner logarithmic boundary layer and the outer Ekman-like layer such that the law-of-the-wall still provides a useful approximation for determining C_{io}. Likely, the use of a smaller reference depth that is closer to the base of the logarithmic boundary layer may increase the accuracy of the quadratic drag assumption (e.g., Park & Stewart, 2016, suggest a hybrid Rossby Similarity Theory using the quadratic drag law to model the inner boundary layer coupled to classic Ekman-layer dynamics for the outer layer).

5.2 Implications for momentum transfer into the ocean

We have focused on the efficiency of momentum transfer between the sea ice and the upper ocean; however, these questions exist in a broader context of the impact of sea ice on mediating total momentum flux between the ocean and the atmosphere. Conventional wisdom has been that sea ice damps atmosphere-ocean momentum flux (Plueddemann et al., 1998; Rainville & Woodgate, 2009), and so an increase in open water will lead to an increase in momentum flux into the ocean (Rainville et al., 2011). However, other recent studies have suggested a more complex view (Martin et al., 2014, 2016; Dosser & Rainville, 2016). Martin et al. (2014, 2016) show that sea ice can either enhance or diminish momentum flux into the ocean depending on the interplay between internal ice stress and wind stress (which is amplified over the sea ice; e.g., Guest et al., 1995, and many others). A detailed accounting of the upper ocean response to the combined sea ice and atmospheric forcing is outside the scope of the current study; here we consider the potential for amplification or damping of momentum flux into the ocean by sea ice.

The equivalent drag coefficient, C_{equiv} (eq. 6) provides a measure of the total momentum transfer efficiency between the atmosphere and the ocean as it is mediated by sea ice. To provide additional context for the observations, consider two limits for the value of C_{equiv}: (1) a "free-drift limit", where $\boldsymbol{F}_a = \boldsymbol{F}_i = 0$ in eq. (5), so $\boldsymbol{\tau}_{ocn} = \boldsymbol{\tau}_{atm}$; (2) the atmosphere-ice stress, $\boldsymbol{\tau}_{ai}$, is balanced by internal ice stress, $\nabla \cdot \boldsymbol{\sigma}$, and $\boldsymbol{F}_a$ is negligible, so $\boldsymbol{\tau}_{io} = 0$. Then for each case the equivalent drag coefficient is given by:

$$\text{case 1:} \qquad C_{equiv} = AC_{ai} + (1 - A)C_{ao}, \tag{14a}$$

$$\text{case 2:} \qquad C_{equiv} = (1 - A)C_{ao}. \tag{14b}$$

Taking C_{ao} as constant (an appropriate approximation for typical wind speeds), the two cases above provide formula for C_{equiv} that are functions solely of ice concentration (noting application of an ice-concentration based parameterization scheme for C_{ai}). While these two cases are referred to as limits, they are not strict limits as both the role of acceleration terms ($\boldsymbol{F}_a$) and the vector addition of terms in eq. (5) can either increase or decrease C_{equiv} beyond these bounds.

Values of C_{equiv} span a wide range, and the variability of observed values increases with increasing sea ice concentration (fig. 11). This increase in variability of C_{equiv} with A reflects the divergence of the two limits of C_{equiv} introduced above, which both approach C_{ao} as $A \to 0$ but either increase (eq. 14a) or decrease (eq. 14b) as A increases. Results also show a separation of C_{equiv} based on the wind factor ($|\boldsymbol{u}_i|/|\boldsymbol{u}_a|$). Points with a wind factor $\geq 2\%$ (defined as being in free drift) generally fall near the upper "free-drift limit" (as expected). This limit shows that in the absence of acceleration terms ($\boldsymbol{F}_a$), ice in free drift will amplify the efficiency of stress transfer compared to open water; how-

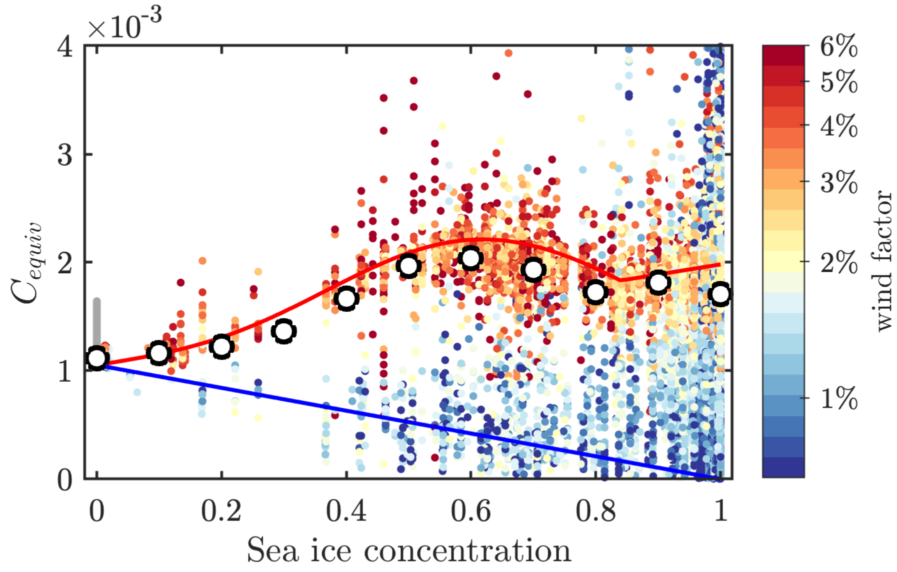

Figure 11: Equivalent drag coefficient C_{equiv} (eq. 6) as a function sea ice concentration (from ERA5). Points shows all hourly values from all moorings, coloured by wind factor (log-scale; grey points had no measurable $\boldsymbol{u}_i$), while black circles show bin-median values by sea ice concentration. The red and blue lines shows the limit cases discussed in the text: red is eq. (14a); blue is eq. (14b).

ever, as $\boldsymbol{F}_a$ also includes the Coriolis acceleration, $\boldsymbol{F}_a$ is non-zero even at steady-state. Points with wind factor below 2% cover a more broad range of values, but for low values (wind factor $\leq$ 1%), C_{equiv} are generally bounded by eq. (14b). This shows that, as expected, the ice interaction force $\boldsymbol{F}_i$ causes a reduction in momentum transfer relative to open-water conditions. Whether the net effect of the ice is to amplify or damp momentum transfer ultimately depends on the strength of this force.

Annual median values of C_{equiv} were similar for each of the three mooring locations with a slight north-south trend: 1.69×10^{-3}, 1.44×10^{-3}, 1.34×10^{-3} for SODA-A, -B, and -C, respectively. This similarity reflects that increased open-water areas (which have a lower efficiency of momentum transfer) at the southern moorings may partly offset expected increases in winter C_{equiv} due to free-drift conditions. However, because wind forcing also has strong seasonal variations with a winter maximum (e.g., Dosser & Rainville, 2016), long-term trends in the total momentum flux into the ocean ($\boldsymbol{\tau}_{ocn}$) will depend both on a balance of increasing open-water conditions and changing internal stress conditions in the winter.

Based on the 2%-rule, the wind factor ($|\boldsymbol{u}_i|/|\boldsymbol{u}_a|$) provides a first-order estimate of the extent of free drift conditions at each mooring. While only a rule-of-thumb, measured values of the wind factor showed asymptotic behaviour supporting use of this rule: as the wind speed increased (i.e., as $\boldsymbol{\tau}_{ai}$ becomes a dominant term in the force balance), wind factor values converged around 2%; bin-average values of the wind factor stay approximately near 2% across a wide range of wind speeds (fig. 12a). There was also a relationship between wind factor and sea ice concentration: for concentrations below ∼80%–85%, the wind factor was elevated and generally greater than 2% (fig. 12b). This suggests that an 80%–85% ice-concentration-based limit for defining free drift is an approximation of the 2%-rule, but it may be the case that free drift conditions also occur intermittently for higher ice concentrations (e.g., on short timescales, atmospheric stress may be balanced primarily by only one of either the ice-ocean or ice-ice stresses, as in Steele et al., 1997). The prevalence of wind factor values greater than 2% have a north-south trend, with roughly 66% of measurements designated as being free drift at SODA-A, 54% at SODA-B, and 37% at SODA-C. Dosser and Rainville (2016) previously showed that the wind factor is a useful indicator for atmosphere-ice-ocean momentum transfer. If the differences between SODA-A and SODA-C are indicative of future trends of sea ice (in which more and more of the Arctic is similar to SODA-A) then this suggests the potential for increasing amplification of stress transfer from the atmosphere to the ocean in the Beaufort Sea during winter.

Martin et al. (2014, 2016) suggests that interplay between wind stress enhancement over sea ice and internal ice stresses (i.e., the relative sizes of $\boldsymbol{\tau}_{atm}$ and $\boldsymbol{F}_i$ in eq. 5) lead to a local maximum in the normalized $\boldsymbol{\tau}_{ocn}$ at some optimal sea ice concentration (their results suggest ∼80 % to 90 %). We see similar evidence for an optimal sea ice concentration in C_{equiv}; binned-median values of C_{equiv} have a peak near 60% ice concentration (fig. 11). However, our observations show that binned-median C_{equiv} roughly follow the free-drift limit (case 1), and there is not an appreciable decrease below that limit in median C_{equiv} at 100% ice concentration (which is in contrast to the pan-Arctic average results presented by Martin et al., 2014). This suggests that the optimal ice concentration for momentum transfer seen in our results is driven by the maximum of eq. (14a), and is minimally affected the ice interaction force ($\boldsymbol{F}_i$). As such, results for optimal ice

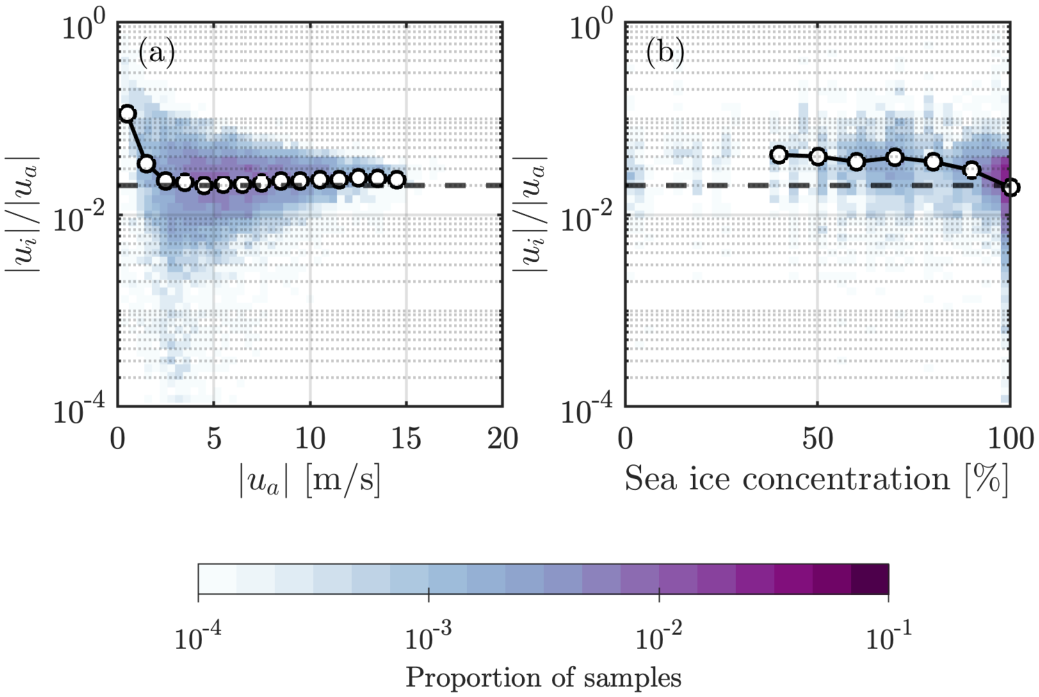

Figure 12: Wind factor ($|\boldsymbol{u}_i|/|\boldsymbol{u}_a|$) as a function of (a) wind speed, and (b) sea ice concentration (from ERA5). In both panels, shading shows a 2-dimensional histogram of the proportion of total samples (on a log-scale), while black lines with circles show the values of wind factor bin-averaged by (a) wind speed, and (b) sea ice concentration. Bin-averages in (b) were only produced for sea ice concentration $\geq$40% due to data scarcity for lower ice concentrations. The horizontal dashed black line in both panels corresponds to a wind factor of 2%.

concentration will be highly sensitive to the parameterization of C_{ia}. Furthermore, these results indicate that, on average, at all three moorings the presences of sea ice causes an amplification of stress transfer compared to open-water conditions for a given wind speed. This is consistent with Martin et al. (2016), who found that sea ice in the Beaufort Sea causes a mean amplification of stress into the ocean for all seasons regardless of whether a constant or variable ice-ocean drag coefficient was used in the model (see their figure 12).

6 Conclusions

Using a force-balance approach to estimate the ice ocean drag coefficient, C_{io}, the annual cycle of the efficiency of ice-ocean momentum transfer is inferred from mooring observations. These estimates compare favorably with drag coefficients using parameterization schemes, based on measured statistics of ice geometry, as well as with previous observations of ice-ocean drag. We summarize the main contributions of the study as follows:

1. The ice ocean drag coefficient, C_{io}, varied seasonally. Variations were more pronounced for the moorings in the seasonal ice zone compared to the mooring that was ice-covered through the full year (fig. 6), suggesting that the enhanced seasonality of the Arctic ice pack is directly influencing seasonality in C_{io}. This manifested as a decrease in C_{io} in the summer and fall, driven by changes in intensity of ridged ice (fig. 8). Wintertime mean values of C_{io} were similar to, or higher than, the canonical value of 5.5×10^{-3} (up to a maximum of 12.3×10^{-3}), but summer and fall values at SODA-A and -B (which may be more representative of future conditions) were as low as $\sim 1.3 \times 10^{-3}$ (fig. 10). The observed seasonality agrees with previous observational studies in the Western Arctic (Cole et al., 2017; Dewey, 2019), but contrast with pan-Arctic model results (Tsamados et al., 2014; Martin et al., 2016).
2. Geometry-based drag parameterizations reproduce many of the spatial and temporal variations of ice-ocean drag, provided that the ice geometry is known (figs. 6 and 7). Slight modifications to the existing parameterization schemes produces the most favourable results (T14(II); fig. 7c), but a full optimization of all free parameters has yet to be performed (and should account for non-neutral conditions

and differences in boundary layer structure). Parameterization of the ice geometry (T14(III)) appears more challenging (fig. 7d), particularly predicting the correct floe sizes (impacting the total floe edge drag, figs. 8d to 8f). The mismatch in seasonality of ice-ocean drag between observations (Cole et al., 2017; Dewey, 2019, and the present study) and models (Tsamados et al., 2014; Martin et al., 2016) is likely a direct result of the difficulties in predicting floe aspect ratios using bulk parameters.

3. In the seasonal ice zone, ridging intensity grows relatively slowly compared to the growth of ice concentration (compare figs. 2d and 2e with fig. 5f). As a result, it is unlikely that simplified parameterization schemes based solely on ice concentration (such have been suggested for atmospheric drag; e.g., Andreas, Horst, et al., 2010; Andreas, Persson, et al., 2010) will be able to adequately capture variations in ice-ocean drag during the ice growth season.
4. The presence of sea ice causes a net amplification of the efficiency of stress input to the ocean compared to open water (section 5.2) which we attribute to the prevalence of free drift conditions (including intermittently during full ice cover). Our measurements support the notion of an "optimal ice concentration" for momentum transfer (Martin et al., 2014, 2016), but suggest the value of the optimal concentration has high sensitivity to the parameterization of the atmosphere-ice drag coefficient, C_{ai} (fig. 11). A comparison between moorings indicates that free drift conditions are more common to the south, and thus may become more common throughout the Beaufort Sea in the future, with a net trend of amplified coupling between the atmosphere and the ocean.

The capability of models to represent the coupled atmosphere-ice-ocean system continues to evolve. Despite mismatches in predictions of ice geometry statistics which are used as inputs, the general success of the parameterization schemes described here gives greater confidence in our ability to use modelled results to learn about the "new Arctic", provided that methods can be developed to account for those mismatches. New sea-ice modelling schemes may be able to directly represent floe size distributions (Roach et al., 2018) or keel statistics (Roberts et al., 2019), reducing the need to redefine parameterizations of sea ice geometry. As model parameterizations of ice-ocean drag evolve, it will become important for users who apply those schemes to choose a framework that matches the model application, including an appropriate choice of reference depth, z_{ref}.

For example, for an upper-ocean mixing study that uses $\boldsymbol{\tau}_{io}$ as a surface boundary condition it may be most appropriate to use a value of C_{io} consistent with drag at the base of the surface log-layer, or to choose z_{ref} in eq. (8) corresponding to the shallowest resolved ocean model level. Drag in a large-scale ice drift model driven by geostrophic ocean currents may be better described by Rossby Similarity Theory (Blackadar & Tennekes, 1968; McPhee, 2008) than by a quadratic drag law; though linking the "effective" roughness length used in that theory to statistics of large scale geometric features remains an open problem. Finally, differences between drag values measured at the different mooring sites indicates that variations in ice morphology may lead to large-scale spatial gradients in the ice-ocean drag, and consequently the surface momentum flux into the ocean, which may have important consequences for studies of large-scale Beaufort Sea circulation (e.g., gyre equilibrium and freshwater storage; Meneghello et al., 2018; Timmermans et al., 2018; Armitage et al., 2020).

Acknowledgments

This work was supported by the Office of Naval Research as part of the Stratified Ocean Dynamics of the Arctic (SODA) research project. Funding was through grant numbers N00014-16-1-2349, N00014-14-1-2377, N00014-18-1-2687. and N00014-16-1-2381. Data files containing the timeseries of the measurements and results described in this study, including sea ice momentum terms, sea ice geometry and ice-ocean drag coefficients, will be made available at `https://digital.lib.washington.edu/researchworks/handle/1773/15609`. More information about the project can be found at `www.apl.washington.edu/soda`. We thank Captain Greg Tlapa and Captain MaryEllen Durley, along with the rest of the command team and crew of USCGC Healy for operational support in 2018 and 2019. This work has benefited from ideas and feedback from members of the SODA project team. We would also like to thank Sarah Dewey for helpful views and conversations.

References

Andreas, E. L. (2011). A relationship between the aerodynamic and physical roughness of winter sea ice. *Quarterly Journal of the Royal Meteorological Society*, *137*(659), 1581–1588. doi: 10.1002/qj.842

Andreas, E. L., Horst, T. W., Grachev, A. A., Persson, P. O. G., Fairall, C. W., Guest, P. S., & Jordan, R. E. (2010, April). Parametrizing turbulent exchange over summer sea ice and the marginal ice zone. *Q.J.R. Meteorol. Soc.*, *136*(649), 927–943. doi: 10.1002/qj.618

Andreas, E. L., Persson, P. O. G., Grachev, A. A., Jordan, R. E., Horst, T. W., Guest, P. S., & Fairall, C. W. (2010, February). Parameterizing Turbulent Exchange over Sea Ice in Winter. *J. Hydrometeor.*, *11*(1), 87–104. doi: 10.1175/2009JHM1102.1

Armitage, T. W. K., Bacon, S., Ridout, A. L., Petty, A. A., Wolbach, S., & Tsamados, M. (2017, July). Arctic Ocean surface geostrophic circulation 2003-2014. *The Cryosphere*, *11*(4), 1767–1780. doi: 10.5194/tc-11-1767-2017

Armitage, T. W. K., Manucharyan, G. E., Petty, A. A., Kwok, R., & Thompson, A. F. (2020, December). Enhanced eddy activity in the Beaufort Gyre in response to sea ice loss. *Nat Commun*, *11*(1), 761. doi: 10.1038/s41467-020-14449-z

Arya, S. P. S. (1975, August). A drag partition theory for determining the large-scale roughness parameter and wind stress on the Arctic pack ice. *J. Geophys. Res.*, *80*(24), 3447–3454. doi: 10.1029/JC080i024p03447

Bendat, J. S., & Piersol, A. G. (1971). *Random data: Analysis and measurement procedures.* New York: Wiley-Interscience.

Blackadar, A. K., & Tennekes, H. (1968). Asymptotic similarity in the neutral barotropic planetary boundary layer. *Journal of the Atmospheric Sciences*, *25*(6), 1015–1020. doi: 10.1175/1520-0469(1968)025⟨1015:ASINBP⟩2.0.CO;2

Brenner, S., Rainville, L., Thomson, J., & Lee, C. (2020). The evolution of a shallow front in the Arctic marginal ice zone. *Elem Sci Anth*(8), 17. doi: 10.1525/elementa.413

Castellani, G., Gerdes, R., Losch, M., & Lüpkes, C. (2015). Impact of Sea-Ice Bottom Topography on the Ekman Pumping. In G. Lohmann, H. Meggers, V. Unnithan, D. Wolf-Gladrow, J. Notholt, & A. Bracher (Eds.), *Towards an Interdisciplinary Approach in Earth System Science: Advances of a Helmholtz Graduate Research School* (pp. 139–148). Cham: Springer International Publishing. doi: 10.1007/978-3-319-13865-7_16

Castellani, G., Losch, M., Ungermann, M., & Gerdes, R. (2018, August). Sea-ice drag as a function of deformation and ice cover: Effects on simulated sea ice and ocean circulation in the Arctic. *Ocean Modelling*, *128*, 48–66. doi: 10.1016/j.ocemod.2018.06.002

Castellani, G., Lüpkes, C., Hendricks, S., & Gerdes, R. (2014, October). Variability of Arctic sea-ice topography and its impact on the atmospheric surface drag. *J. Geophys. Res. Oceans*, *119*(10), 6743–6762. doi: 10.1002/2013JC009712

Cole, S. T., Timmermans, M.-L., Toole, J. M., Krishfield, R. A., & Thwaites, F. T. (2014, May). Ekman Veering, Internal Waves, and Turbulence Observed under Arctic Sea Ice. *J. Phys. Oceanogr.*, *44*(5), 1306–1328. doi: 10.1175/JPO-D-12-0191.1

Cole, S. T., Toole, J. M., Lele, R., Timmermans, M.-L., Gallaher, S. G., Stanton, T. P., . . . Thomson, J. (2017, September). Ice and ocean velocity in the Arctic marginal ice zone: Ice roughness and momentum transfer. *Elem Sci Anth*, *5*, 55. doi: 10.1525/elementa.241

Connolley, W. M., Gregory, J. M., Hunke, E. C., & Mclaren, A. J. (2004). On the consistent scaling of terms in the sea-ice dynamics equation. *JOURNAL OF PHYSICAL OCEANOGRAPHY*, *34*, 5.

Dewey, S. (2019). *Evolving ice-ocean dynamics of the western Arctic* (Unpublished doctoral dissertation). University of Washington.

Dewey, S., Morison, J., Kwok, R., Dickinson, S., Morison, D., & Andersen, R. (2018, February). Arctic ice-ocean coupling and gyre equilibration observed with remote sensing. *Geophys. Res. Lett.*, *45*(3), 1499–1508. doi: 10.1002/2017GL076229

Dosser, H. V., & Rainville, L. (2016, February). Dynamics of the Changing Near-Inertial Internal Wave Field in the Arctic Ocean. *J. Phys. Oceanogr.*, *46*(2), 395–415. doi: 10.1175/JPO-D-15-0056.1

ECMWF. (2019). Part IV: Physical Processes. In *IFS Documentation CY46R1.* ECMWF.

Elvidge, A. D., Renfrew, I. A., Weiss, A. I., Brooks, I. M., Lachlan-Cope, T. A., & King, J. C. (2016, February). Observations of surface momentum exchange over the marginal ice zone and recommendations for its parametrisation. *Atmos. Chem. Phys.*, *16*(3), 1545–1563. doi: 10.5194/acp-16-1545-2016

Graham, R. M., Cohen, L., Ritzhaupt, N., Segger, B., Graversen, R. G., Rinke, A., . . . Hudson, S. R. (2019, July). Evaluation of Six Atmospheric Reanalyses over

Arctic Sea Ice from Winter to Early Summer. *J. Climate*, *32*(14), 4121–4143. doi: 10.1175/JCLI-D-18-0643.1

Guest, P. S., & Davidson, K. L. (1987). The effect of observed ice conditions on the drag coefficient in the summer East Greenland Sea Marginal Ice Zone. *J. Geophys. Res.*, *92*(C7), 6943. doi: 10.1029/JC092iC07p06943

Guest, P. S., Glendening, J. W., & Davidson, K. L. (1995). An observational and numerical study of wind stress variations within marginal ice zones. *J. Geophys. Res.*, *100*(C6), 10887. doi: 10.1029/94JC03391

Harding, S., Kilcher, L., & Thomson, J. (2017, June). Turbulence Measurements from Compliant Moorings. Part I: Motion Characterization. *J. Atmos. Oceanic Technol.*, *34*(6), 1235–1247. doi: 10.1175/JTECH-D-16-0189.1

Heorton, H. D. B. S., Tsamados, M., Cole, S. T., Ferreira, A. M. G., Berbellini, A., Fox, M., & Armitage, T. W. K. (2019, August). Retrieving sea ice drag coefficients and turning angles from in situ and satellite observations using an inverse modeling framework. *J. Geophys. Res. Oceans*, *124*(8), 6388–6413. doi: 10.1029/2018JC014881

Hersbach, H., Bell, B., Berrisford, P., Hirahara, S., Horányi, A., Muñoz-Sabater, J., ... Thépaut, J.-N. (2020). The ERA5 global reanalysis. *Quarterly Journal of the Royal Meteorological Society*, *146*(730), 1999–2049. doi: 10.1002/qj.3803

Holton, J. R. (2004). *An introduction to dynamic meteorology* (4th ed ed.) (No. v. 88). Burlington, MA: Elsevier Academic Press.

Hunke, E. C. (2010, January). Thickness sensitivities in the CICE sea ice model. *Ocean Modelling*, *34*(3), 137–149. doi: 10.1016/j.ocemod.2010.05.004

Hunke, E. C., Allard, R., Bailey, D. A., Blain, P., Craig, A., Dupont, F., ... Winton, M. (2020, June). *CICE-Consortium/CICE: CICE Version 6.1.2.* Zenodo. doi: 10.5281/zenodo.3888653

Hunke, E. C., & Dukowicz, J. K. (2003). The sea ice momentum equation in the free drift regime. , 10.

Hunkins, K. (1966, August). Ekman drift currents in the Arctic Ocean. *Deep Sea Research and Oceanographic Abstracts*, *13*(4), 607–620. doi: 10.1016/0011-7471(66)90592-4

Ivanov, V., Alexeev, V., Koldunov, N. V., Repina, I., Sandø, A. B., Smedsrud, L. H., & Smirnov, A. (2016, May). Arctic Ocean Heat Impact on Regional Ice Decay:

A Suggested Positive Feedback. *J. Phys. Oceanogr.*, *46* (5), 1437–1456. doi: 10.1175/JPO-D-15-0144.1

Jackson, J. M., Allen, S. E., McLaughlin, F. A., Woodgate, R. A., & Carmack, E. C. (2011). Changes to the near-surface waters in the Canada Basin, Arctic Ocean from 1993–2009: A basin in transition. *Journal of Geophysical Research: Oceans*, *116* (C10). doi: 10.1029/2011JC007069

Johannessen, O. M. (1970). Note on some vertical profiles below ice floes in the Gulf of St. Lawrence and near the North Pole. *Journal of Geophysical Research (1896-1977)*, *75* (15), 2857–2861. doi: 10.1029/JC075i015p02857

Kim, J. G., Hunke, E. C., & Lipscomb, W. H. (2006, January). Sensitivity analysis and parameter tuning scheme for global sea-ice modeling. *Ocean Modelling*, *14* (1), 61–80. doi: 10.1016/j.ocemod.2006.03.003

Kim, T. W., Ha, H. K., Wåhlin, A. K., Lee, S. H., Kim, C. S., Lee, J. H., & Cho, Y. K. (2017, January). Is Ekman pumping responsible for the seasonal variation of warm circumpolar deep water in the Amundsen Sea? *Continental Shelf Research*, *132*, 38–48. doi: 10.1016/j.csr.2016.09.005

Kirillov, S., Babb, D., Dmitrenko, I., Landy, J., Lukovich, J., Ehn, J., ... Stroeve, J. (2020, February). Atmospheric forcing drives the winter sea ice thickness asymmetry of Hudson Bay. *J. Geophys. Res. Oceans*, *125* (2). doi: 10.1029/2019JC015756

Köberle, C., & Gerdes, R. (2003, September). Mechanisms Determining the Variability of Arctic Sea Ice Conditions and Export. *J. Climate*, *16* (17), 2843–2858. doi: 10.1175/1520-0442(2003)016⟨2843:MDTVOA⟩2.0.CO;2

Krishfield, R. A., Proshutinsky, A., Tateyama, K., Williams, W. J., Carmack, E. C., McLaughlin, F. A., & Timmermans, M.-L. (2014, February). Deterioration of perennial sea ice in the Beaufort Gyre from 2003 to 2012 and its impact on the oceanic freshwater cycle. *J. Geophys. Res. Oceans*, *119* (2), 1271–1305. doi: 10.1002/2013JC008999

Large, W. G., & Yeager, S. G. (2004). *Diurnal to decadal global forcing for ocean and sea-ice models: The data sets and flux climatologies* (Technical Note Nos. NCAR/TN-460+STR). Boulder Colorado: National Center for Atmospheric Research.

Leppäranta, M. (2011). *The drift of sea ice* (M. Leppäranta, Ed.). Berlin, Heidelberg: Springer. doi: 10.1007/978-3-642-04683-4_2

Losch, M., Menemenlis, D., Campin, J.-M., Heimbach, P., & Hill, C. (2010, January). On the formulation of sea-ice models. Part 1: Effects of different solver implementations and parameterizations. *Ocean Modelling*, *33*(1-2), 129–144. doi: 10.1016/j.ocemod.2009.12.008

Lu, P., Li, Z., Cheng, B., & Leppäranta, M. (2011, July). A parameterization of the ice-ocean drag coefficient. *J. Geophys. Res.*, *116*(C7), C07019. doi: 10.1029/2010JC006878

Lüpkes, C., & Birnbaum, G. (2005, November). Surface drag in the Arctic marginal sea-ice zone: A comparison of different parameterisation concepts. *Boundary-Layer Meteorol*, *117*(2), 179–211. doi: 10.1007/s10546-005-1445-8

Lüpkes, C., & Gryanik, V. M. (2015). A stability-dependent parametrization of transfer coefficients for momentum and heat over polar sea ice to be used in climate models. *Journal of Geophysical Research: Atmospheres*, *120*(2), 552–581. doi: 10.1002/2014JD022418

Lüpkes, C., Gryanik, V. M., Hartmann, J., & Andreas, E. L. (2012, July). A parametrization, based on sea ice morphology, of the neutral atmospheric drag coefficients for weather prediction and climate models. *J. Geophys. Res.*, *117*(D13), n/a-n/a. doi: 10.1029/2012JD017630

Magnell, B., Ivanov, L., & Siegel, E. (2010, September). Measurements of ice parameters in the Beaufort Sea using the Nortek AWAC acoustic Doppler current profiler. In *OCEANS 2010 MTS/IEEE SEATTLE* (pp. 1–8). doi: 10.1109/OCEANS.2010.5664016

Martin, T. (2007). *Arctic sea ice dynamics: Drift and ridging in numerical models and observations* (Unpublished doctoral dissertation). University of Bremen.

Martin, T., Steele, M., & Zhang, J. (2014, March). Seasonality and long-term trend of Arctic Ocean surface stress in a model. *J. Geophys. Res. Oceans*, *119*(3), 1723–1738. doi: 10.1002/2013JC009425

Martin, T., Tsamados, M., Schroeder, D., & Feltham, D. L. (2016, March). The impact of variable sea ice roughness on changes in Arctic Ocean surface stress: A model study. *J. Geophys. Res. Oceans*, *121*(3), 1931–1952. doi: 10.1002/2015JC011186

McPhee, M. G. (1979, March). The Effect of the Oceanic Boundary Layer on the

Mean Drift of Pack Ice: Application of a Simple Model. *J. Phys. Oceanogr.*, *9*(2), 388–400. doi: 10.1175/1520-0485(1979)009⟨0388:TEOTOB⟩2.0.CO;2

McPhee, M. G. (1980). An analysis of pack ice drift in summer. , 14.

McPhee, M. G. (2002). Turbulent stress at the ice/ocean interface and bottom surface hydraulic roughness during the SHEBA drift. *J. Geophys. Res.*, *107*(C10), 8037. doi: 10.1029/2000JC000633

McPhee, M. G. (2008). *Air-ice-ocean interaction: Turbulent ocean boundary layer exchange processes*. New York: Springer-Verlag. doi: 10.1007/978-0-387-78335-2

McPhee, M. G. (2012, June). Advances in understanding ice–ocean stress during and since AIDJEX. *Cold Regions Science and Technology*, *76-77*, 24–36. doi: 10.1016/j.coldregions.2011.05.001

McPhee, M. G., & Kantha, L. H. (1989). Generation of internal waves by sea ice. *J. Geophys. Res.*, *94*(C3), 3287. doi: 10.1029/JC094iC03p03287

McPhee, M. G., Kottmeier, C., & Morison, J. H. (1999, June). Ocean Heat Flux in the Central Weddell Sea during Winter. *J. Phys. Oceanogr.*, *29*(6), 1166–1179. doi: 10.1175/1520-0485(1999)029⟨1166:OHFITC⟩2.0.CO;2

Meneghello, G., Marshall, J., Campin, J.-M., Doddridge, E., & Timmermans, M.-L. (2018). The Ice-Ocean Governor: Ice-Ocean Stress Feedback Limits Beaufort Gyre Spin-Up. *Geophysical Research Letters*, *45*(20), 11,293–11,299. doi: 10.1029/2018GL080171

Morison, J. H., McPhee, M. G., & Maykut, G. A. (1987). Boundary layer, upper ocean, and ice observations in the Greenland Sea Marginal Ice Zone. *Journal of Geophysical Research: Oceans*, *92*(C7), 6987–7011. doi: 10.1029/JC092iC07p06987

Park, H.-S., & Stewart, A. L. (2016, January). An analytical model for wind-driven Arctic summer sea ice drift. *The Cryosphere*, *10*(1), 227–244. doi: 10.5194/tc-10-227-2016

Perrie, W., & Hu, Y. (1997). Air–ice–ocean momentum exchange. Part II: Ice drift. *JOURNAL OF PHYSICAL OCEANOGRAPHY*, *27*, 21.

Petty, A. A., Tsamados, M. C., & Kurtz, N. T. (2017, August). Atmospheric form drag coefficients over Arctic sea ice using remotely sensed ice topography data, spring 2009-2015. *J. Geophys. Res. Earth Surf.*, *122*(8), 1472–1490. doi:

10.1002/2017JF004209

Pite, H. D., Topham, D. R., & van Hardenberg, B. J. (1995, December). Laboratory measurements of the drag force on a family of two-dimensional ice keel models in a two-layer flow. *J. Phys. Oceanogr.*, *25* (12), 3008–3031. doi: 10.1175/1520-0485(1995)025⟨3008:LMOTDF⟩2.0.CO;2

Plueddemann, A. J., Krishfield, R., Takizawa, T., Hatakeyama, K., & Honjo, S. (1998). Upper ocean velocities in the Beaufort Gyre. *Geophysical Research Letters*, *25* (2), 183–186. doi: 10.1029/97GL53638

Rainville, L., Lee, C., & Woodgate, R. A. (2011). Impact of wind-driven mixing in the Arctic Ocean. *Oceanography*, *24* (3), 136–145.

Rainville, L., & Woodgate, R. A. (2009, December). Observations of internal wave generation in the seasonally ice-free Arctic. *Geophys. Res. Lett.*, *36* (23), L23604. doi: 10.1029/2009GL041291

Rampal, P., Bouillon, S., Ólason, E., & Morlighem, M. (2016, May). NeXtSIM: A new Lagrangian sea ice model. *Cryosphere*, *10* (3), 1055–1073. doi: 10.5194/tc-10-1055-2016

Randelhoff, A., Sundfjord, A., & Renner, A. H. H. (2014, August). Effects of a shallow pycnocline and surface meltwater on sea ice–ocean drag and turbulent heat flux. *J. Phys. Oceanogr.*, *44* (8), 2176–2190. doi: 10.1175/JPO-D-13-0231.1

Roach, L. A., Horvat, C., Dean, S. M., & Bitz, C. M. (2018). An Emergent Sea Ice Floe Size Distribution in a Global Coupled Ocean-Sea Ice Model. *Journal of Geophysical Research: Oceans*, *123* (6), 4322–4337. doi: 10.1029/2017JC013692

Roberts, A. F., Hunke, E. C., Kamal, S. M., Lipscomb, W. H., Horvat, C., & Maslowski, W. (2019, March). A variational method for sea ice ridging in earth system models. *J. Adv. Model. Earth Syst.*, *11* (3), 771–805. doi: 10.1029/2018MS001395

Rousset, C., Vancoppenolle, M., Madec, G., Fichefet, T., Flavoni, S., Barthélemy, A., ... Vivier, F. (2015). The Louvain-La-Neuve sea ice model LIM3.6: Global and regional capabilities. *Geoscientific Model Development*, *8*, 2991–3005. doi: 10.5194/gmd-8-2991-2015

Shaw, W. J., Stanton, T. P., McPhee, M. G., & Kikuchi, T. (2008, August). Estimates of surface roughness length in heterogeneous under-ice boundary layers.

J. Geophys. Res., *113*(C8), C08030. doi: 10.1029/2007JC004550

Shcherbina, A., D'Asaro, E. A., Light, B., Deming, J. W., & Rehm, E. (2016, February). *Maiden Voyage of the Under-Ice Float.*

Shirasawa, K., & Ingram, R. G. (1991, July). Characteristics of the turbulent oceanic boundary layer under sea ice. Part 1: A review of the ice-ocean boundary layer. *Journal of Marine Systems*, *2*(1), 153–160. doi: 10.1016/0924-7963(91)90021-L

Shirasawa, K., Ingram, R. G., & Aota, M. (1989). Measurements in the boundary layer under landfast ice in the southeast Hudson Bay, Canada. *Low Temperature Science*, *A*(47), 213–221.

Spreen, G., Kaleschke, L., & Heygster, G. (2008). Sea ice remote sensing using AMSR-E 89-GHz channels. *Journal of Geophysical Research: Oceans*, *113*(C2). doi: 10.1029/2005JC003384

Steele, M., Morison, J. H., & Untersteiner, N. (1989). The partition of air-ice-ocean momentum exchange as a function of ice concentration, floe size, and draft. *J. Geophys. Res.*, *94*(C9), 12739. doi: 10.1029/JC094iC09p12739

Steele, M., Zhang, J., Rothrock, D., & Stern, H. (1997, September). The force balance of sea ice in a numerical model of the Arctic Ocean. *J. Geophys. Res.*, *102*(C9), 21061–21079. doi: 10.1029/97JC01454

Steiner, N. (2001). Introduction of variable drag coefficients into sea-ice models. *Ann. Glaciol.*, *33*, 181–186. doi: 10.3189/172756401781818149

Stern, H. L., Schweiger, A. J., Zhang, J., & Steele, M. (2018, July). On reconciling disparate studies of the sea-ice floe size distribution. *Elem Sci Anth*, *6*(1), 49. doi: 10.1525/elementa.304

Stroeve, J., & Notz, D. (2018, September). Changing state of Arctic sea ice across all seasons. *Environ. Res. Lett.*, *13*(10), 103001. doi: 10.1088/1748-9326/aade56

Timmermann, R., Danilov, S., Schröter, J., Böning, C., Sidorenko, D., & Rollenhagen, K. (2009, January). Ocean circulation and sea ice distribution in a finite element global sea ice–ocean model. *Ocean Modelling*, *27*(3-4), 114–129. doi: 10.1016/j.ocemod.2008.10.009

Timmermans, M.-L., Toole, J., & Krishfield, R. (2018, August). Warming of the interior Arctic Ocean linked to sea ice losses at the basin margins. *Sci. Adv.*, *4*(8), eaat6773. doi: 10.1126/sciadv.aat6773

Tsamados, M., Feltham, D. L., Schroeder, D., Flocco, D., Farrell, S. L., Kurtz, N., . . . Bacon, S. (2014, May). Impact of variable atmospheric and oceanic form drag on simulations of Arctic sea ice. *J. Phys. Oceanogr.*, *44*(5), 1329–1353. doi: 10.1175/JPO-D-13-0215.1

Wadhams, P., & Davy, T. (1986). On the spacing and draft distributions for pressure ridge keels. *J. Geophys. Res.*, *91*(C9), 10697. doi: 10.1029/JC091iC09p10697

Wadhams, P., & Horne, R. J. (1980). An Analysis Of Ice Profiles Obtained By Submarine Sonar In The Beaufort Sea. *J. Glaciol.*, *25*(93), 401–424. doi: 10.3189/S0022143000015264

Weiss, J., & Marsan, D. (2004, September). Scale properties of sea ice deformation and fracturing. *Comptes Rendus Physique*, *5*(7), 735–751. doi: 10.1016/j.crhy.2004.09.005

Williams, E., Swithinbank, C., & Robin, G. d. Q. (1975). A submarine sonar study of Arctic pack ice. *Journal of Glaciology*, *15*(73), 349–362. doi: 10.3189/S002214300003447X